AIAA JOURNAL
Vol. 49, No. 9, September 2011

Wall-Pressure Sources Near an Airfoil Trailing Edge Under Separated Laminar Boundary Layers

Ana Garcia-Sagrado* and Tom Hynes†
University of Cambridge, Cambridge, England CB3 ODY, United Kingdom

DOI: 10.2514/1.J050477

The wall-pressure sources near the trailing edge of an airfoil due to separated laminar boundary layers developing on the surface have been investigated in the present work. Boundary-layer wall-pressure fluctuations are responsible for flow-induced noise such as the airfoil self-noise mechanism of narrowband noise due to vortex shedding from separated laminar boundary layers. The airfoil used was a NACA0012 of 30 cm chord with an aspect ratio of 1, and the experiments have been done at two different flow conditions (Reynolds number based on the chord: $Re_c = 2 \times 10^5$ and 4×10^5). An aerodynamic investigation was carried out by performing simultaneous measurements of the unsteady surface pressure and velocity fields. Cross-correlations between velocity and surface pressure provided deeper insight into the surface-pressure-generating flow structures. The laminar boundary layer separated in the second half of the airfoil and reattached upstream of the trailing edge for the two chord Reynolds numbers investigated. The vortices from the separated shear layer were tonal in nature for the low Re_c and more broadband for the high Re_c, since the boundary-layer instability waves interacted with additional frequencies from the transition process that started very close to the separation point for the high-Re_c case. These vortices were identified as the dominant wall-pressure-generating structures, and hence the sources of the wall-pressure fluctuations, and were found to be distributed across the boundary layer. Evidence of unsteady vortex shedding was also observed behind the blunt trailing edge.

Nomenclature

C	=	chord and axial chord of the airfoil (they become the same variable at 0° angle of attack), m
C_p	=	pressure coefficient, $(P_{01} - p_s)/(P_{01} - p_{s2})$
f	=	frequency, Hz
h	=	trailing-edge thickness, m
H_{12}	=	shape factor, δ^*/θ
MD	=	separation-bubble maximum displacement point
P_{01}	=	inlet total pressure, Pa
p_o	=	reference pressure equal to 20 μPa
p_{rms}	=	root mean square of pressure fluctuations, Pa
p_s	=	surface static pressure, Pa
p_{s2}	=	exit static pressure, Pa
p'	=	fluctuating surface pressure, Pa
q_e	=	pressure dynamic head based on the velocity at the edge of the boundary layer U_e, m^2/s^2
R	=	separation-bubble reattachment point
R_{up}, R_{vp}	=	temporal cross-correlation coefficient between the streamwise and normal component of the velocity and surface pressure
Re_c	=	Reynolds based on the chord of the airfoil
S	=	separation-bubble separation point
tr	=	separation-bubble onset of transition point
U_c	=	convection velocity, m/s
U_e	=	velocity at the edge of the boundary layer, m/s
U_∞	=	freestream velocity (unless contrary stated, it is the same as $U_{\infty,o}$ and as U_o), m/s
$U_{\infty,i}$	=	freestream velocity at the inlet, upstream of the leading edge at a distance of $0.3C$ and below the midcenterline of the airfoil by $0.25C$, m/s
$U_{\infty,o}$	=	freestream velocity at the outlet, above the trailing edge at a distance equal to $0.3C$, m/s
u_{rms}	=	root mean square of velocity fluctuations, m/s
u', v'	=	turbulent fluctuating velocity components, m/s
x	=	streamwise distance from the airfoil leading edge, m
x'	=	streamwise distance from the airfoil trailing edge, m
y	=	normal distance from the wall or from the airfoil extended centerline, m
z	=	lateral distance from the airfoil midspan, m
δ	=	boundary-layer thickness, m
δ^*	=	boundary-layer displacement thickness, m
θ	=	boundary-layer momentum thickness, m
Λ_θ	=	Pohlhausen pressure-gradient parameter, $(\theta^2/\nu)(\text{d}U_\infty/\text{d}x)$
μ	=	dynamic viscosity, kg/ms
ν	=	kinematic viscosity, m^2/s
ξ_m	=	streamwise position of a selected microphone, m
ξ_o	=	streamwise position of cross wire, m
ρ	=	density, kg/m^3
τ	=	time delay, s
τ_o	=	nondimensional time delay, $\tau U_e/\delta^*$, associated with the period of the unsteady vortex shedding at the trailing edge
Φ, $\Phi(f)$, $\Phi(\omega)$	=	surface-pressure power spectral density, Pa^2/Hz

Received 29 March 2010; revision received 24 March 2011; accepted for publication 25 March 2011.

*Whittle Laboratory; currently Research Associate, Imperial College London, Department of Earth Science and Engineering, Royal School of Mines, Prince Consort Road, London, England SW7 2BP, U.K.

†Reader, Whittle Laboratory, Department of Engineering, 1 J. J. Thomson Avenue. Member AIAA.

I. Introduction

INTEREST in low-Reynolds-number aerodynamics has increased over the last years, due to new applications such as sailplanes, unmanned aerial vehicles and micro air vehicles. In these applications the chord-based Reynolds numbers (Re_c) range from 50,000 to 500,000. The aerodynamic performance of airfoils used for high-speed aircraft (high Re_c) deteriorates when used for low-Reynolds-number applications. At high Re_c, flows are mostly turbulent, whereas at low Re_c, boundary layers remain laminar for a large percentage of the airfoil chord and are prone to separate, due to the

adverse pressure gradient. Once separated, they become highly unstable.

Separated laminar boundary layers transition to turbulent and reattach to the surface when the adverse pressure gradient is moderate, forming a laminar separation bubble. If the adverse pressure gradient is large, for example, when increasing the airfoil angle of attack, the separation bubble bursts. Since such separation brings about significant adverse aerodynamic effects, especially an increase in drag, a good physical understanding is crucial to control laminar boundary-layer separation.

Numerous experimental studies can be found in the literature investigating laminar flow separation, transition, and reattachment on low Re_c, although most of them measure pointwise velocity with hot-wire anemometry (Hatman and Wang [1], Johnson [2] Solomon et al. [3], and Volino and Hultgren [4]) or laser Doppler anemometry (Fitzgerald and Mueller [5], Brendel and Mueller [6], and O'Meara and Mueller [7]). Only a few studies have recently provided simultaneous measurements of velocity at different points to provide spatially resolved flowfield measurements (Lang et al. [8], Ol et al. [9], Raffel et al. [10], and Burgmann et al. [11]). These measurements are necessary to improve the understanding of the underlying physics in these separated-flow scenarios. Little can be found in the literature for which flowfield measurements on airfoils are correlated with airfoil surface pressure. Only recently, in Hu and Yang [12], were velocity measurements from particle image velocimetry taken at the same time as surface-pressure measurements, but these pressure measurements were not time-resolved. Furthermore, Hu and Yang [12] acquired statistical data with the particle image velocimetry measurements instead of time-resolved measurements, due to the limited sampling rates, whereas in the current study the use of cross-wire anemometry and microphones with high sampling rates allowed time-resolved measurements to be analyzed. Hence, the novelty of the present investigation is that unsteady velocity measurements were taken at the same time as unsteady wall-pressure measurements. The complicated interdependence of the flow characteristics at laminar separation, transition, and turbulent reattachment are obstacles to computational models. Good-quality experimental data are therefore also useful to validate these models.

Moreover, improving the understanding of the sources of wall-pressure fluctuations is crucial for many applications such as flow-induced vibrations in ship hulls or flow-induced noise in airfoils, which is relevant for aircraft noise (wings, high-lift devices, and engine turbomachinery blades) and for wind turbine noise. One of the airfoil self-noise mechanisms defined by Brooks et al. [13] is the narrowband and tonal noise due to vortex shedding from the instability waves of a laminar boundary layer or of separated shear layers. Narrowband noise is also generated due to vortex shedding from blunt trailing edges. These are the mechanisms of relevance to this paper.

Airfoil self-noise is produced when an airfoil encounters smooth nonturbulent inflow, due to the vortical disturbances developing in the boundary layers. Roger and Moreau [14] reported that in the generation of broadband noise from turbulent boundary layers and of tonal noise from laminar unstable (or separated) boundary layers, a similar physical process is involved at the trailing edge. Vortical boundary-layer disturbances are partially converted into acoustical ones as they convect past the trailing edge. Therefore, airfoil self-noise is sometimes referred to as airfoil trailing-edge noise. Flow-induced vibration and noise in ship hulls is another example of unwanted phenomena due to the surface-pressure fluctuations generated by the velocity field (Kinns and Bloor [15], Ciappi et al. [16], and Ciappi and Magionesi [17]).

Tonal noise from airfoil trailing edge has been linked to an acoustic-feedback mechanism involving boundary-layer instabilities. This mechanism of tonal noise generation was also recently studied by direct numerical simulations (Desqesnes et al. [18], Sandberg et al. [19], and Jones et al. [20]). The flowfield was reported to be unstable because of an acoustic-feedback loop in which instability waves convecting over the trailing edge generate acoustic waves that propagate upstream and generate further instability waves within the boundary layer. The naturally appearing vortex shedding generates nonlinear disturbances in the separated shear layer by means of the feedback mechanism.

Many authors in the literature such as Howe [21], Amiet [22], Brooks and Hodgson [23], Roger and Moreau [14], and Yu and Joshi [24] and, more recently, Rozenberg et al. [25], Bertagnolio et al. [26], and Wang et al. [27], associate the statistics of the far-field noise with those of the aerodynamic surface pressure upstream of the trailing edge. Wall-pressure and acoustic spectral envelopes are very closely related, indicating a cause-effect relationship.

In the present work, laminar flow separation and the above mentioned airfoil self-noise mechanisms have been investigated from an aerodynamic point of view. The aerodynamic investigation has been carried out by performing simultaneous measurements of the unsteady surface-pressure fluctuations and of the velocity field in the boundary layer and wake of a NACA0012 airfoil, especially in the region close to the trailing edge (TE). This allowed for the calculation of cross-correlations between the two components of the velocity and the surface pressure. These detailed measurements have provided further understanding of the relationship between the velocity and wall-pressure fields and hence of the flow structures responsible for the wall-pressure generation. Furthermore, the analysis of the temporal signals and spectra from the velocity and pressure fluctuations was crucial in the identification of the onset of transition in these separated flows. The results presented in this paper correspond to a blunt TE and the measurements were done at a 0° angle of attack.

II. Experimental Setup

A. Airfoil Model and Experimental Setup

The experimental setup consisted of a NACA0012 airfoil, an open-circuit wind tunnel, Perspex side walls to support the airfoil at the exit of the tunnel, the sensing instrumentation and data-acquisition systems.

At low frequencies, the surface-pressure signals can be contaminated by facility background noise, and therefore the measurements of wall-pressure fluctuations are often carried out in an acoustically quiet wind tunnel or are treated afterward by applying a noise-cancellation technique (Agarwal and Simpson [28], Helal et al. [29], and Naguib et al. [30]). In the present case, measurements were done in different wind tunnels and the most quite wind tunnel was chosen for the experiments. Furthermore, the internal walls of the wind tunnel were covered with a foam material (5 cm thickness) that reduced the background noise of the facility by up to 20 dB from 100 Hz onward. This allowed the measurement of the pressure signature of interest without the need to apply a noise-cancellation technique. Noise-cancellation techniques (Naguib et al. [30]) were applied to the first set of data to assess the quality of the signals. It was found that there was no further improvement by the application of the noise-cancellation methods, and therefore these have not been applied to the data.

This acoustically quiet modified wind tunnel used in the investigation is an open-circuit blower type wind tunnel attached to a 15 kW Siemens fan. It contains a series of grids, gauzes and honeycombs to smooth and settle the flow before passing through a 4:1 area-ratio contraction and discharging into the test section. The exit of the tunnel has a rectangular cross section of 0.38 m by 0.59 m (after the foam). The freestream turbulence intensity of the tunnel is 0.4%, allowing the investigation of the flow around a NACA0012 in a smooth nonturbulent inflow.

As seen in Fig. 1, the airfoil has been placed at the exit of the tunnel (open jet configuration), supported by two Perspex side walls. These are connected to the exit of the tunnel, allowing a gap between them and the tunnel lateral walls of 3 cm in order to remove the boundary layer developing on the walls of the tunnel. The edges of the Perspex walls have been rounded so that the impinging flow flows smoothly around them. Boundary layers developed from the edge of the Perspex side walls as it can be seen in the oil and dye flow visualization pictures shown in Sec. III.D. However, since the measurements were done at midspan, they did not affect the results. This configuration has been broadly used in the literature in the

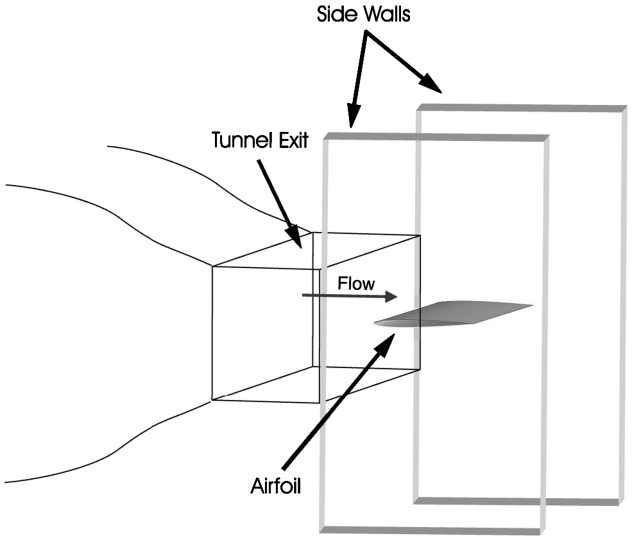

Fig. 1 Simplifying illustration of the exit of the wind tunnel and Perspex side walls holding the airfoil.

investigation of trailing-edge noise (Brooks et al. [13], Brooks and Hodgson [23], Roger and Moreau [14], and Rozenberg et al. [25,31,32]). The distance from the leading edge of the airfoil to the front of the side walls is equal to the airfoil chord, i.e., 300 mm, and from the TE to the end of the side walls is 1.37 times the chord, equal to 410 mm.

The symmetric airfoil employed in the current investigation was a NACA0012 airfoil with a chord of 300 mm and an aspect ratio of 1. As seen in Fig. 2, it consisted of three parts of which the middle one was hollow. This part had a span of 200 mm and was made of three different pieces, allowing the airfoil to be completely dismantled and thus, providing access to the interior in order to place the instrumentation. One of these three pieces formed the TE that was exchangeable to allow different TE geometries to be investigated if needed. The two lateral parts are solid and have a span of 50 mm each. Their length was modified when exchanging the TE, so that it was the same as that of the central part.

The TE thickness h was 1.6 mm and $h/\delta^* > 0.3$, where δ^* is the boundary-layer displacement thickness at the edge. As indicated by Blake [33], this corresponds to a blunt TE, where vortex shedding is then normally observed from the TE. Note that the NACA0012 airfoil was truncated near the TE in order to have a thickness at the TE of 1.6 mm and hence a blunt TE. This resulted in a final chord C of 297 mm.

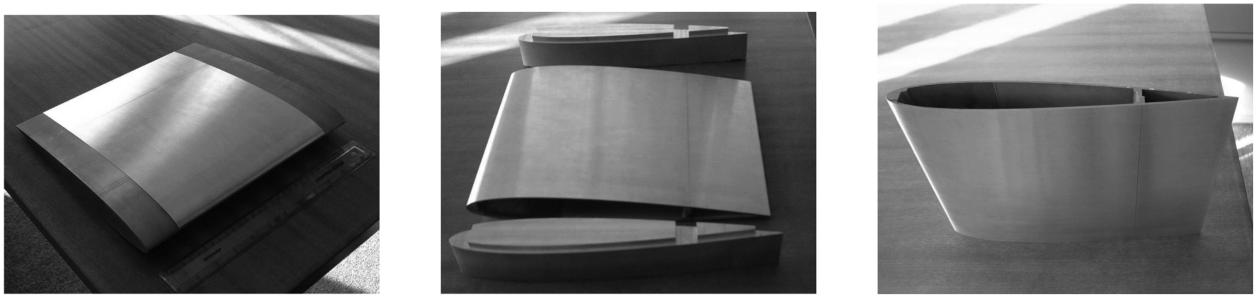

a) **b)** **c)**

Fig. 2 NACA0012 model used for the experiments: a) NACA0012 assembled, b) middle hollow part and lateral solid parts, and c) middle hollow part made of three different pieces (one of them is an exchangeable TE).

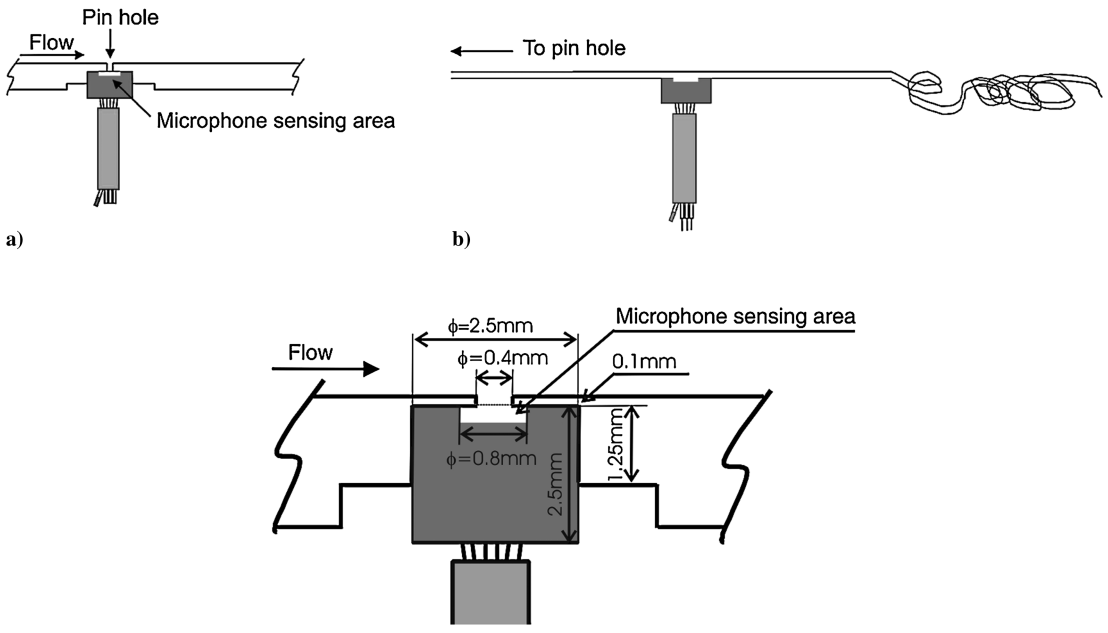

a) **b)**

c)

Fig. 3 Illustrations of a) microphone under a pin-hole configuration, b) remote microphone arrangement, and c) dimensions of microphone and pin-hole configuration.

The experiments were done at two different flow conditions corresponding to two Reynolds numbers, $Re_c = 2 \times 10^5$ and 4×10^5 based on the chord of the airfoil and freestream velocities of 10 and 20 m/s, respectively. No trip wire was placed on the surface of the airfoil, since the aim was to investigate a laminar-separated boundary layer. The investigation was done at a 0° angle of attack (AOA).

B. Model Instrumentation

Static-pressure tappings of 0.3 mm were drilled into the airfoil surface, allowing measurements of the static pressure and thus the calculation of the static-pressure coefficient distribution. Since static tappings were placed on both sides of the airfoil, the alignment of the airfoil with the flow at 0° AOA could be ensured by checking the symmetry of the static-pressure coefficient results.

The microphones selected for the unsteady surface-pressure measurements have been FG-3329-P07 from Knowles Electronics. These are 2.5-mm-diam omnidirectional electret condenser microphones with a circular sensing area of 0.79 mm. They have been embedded in the airfoil under a pin hole of 0.4 mm diameter in order to minimize attenuation effects at high frequencies due to the finite size of the microphones. A microphone under a pin-hole arrangement is depicted in Fig. 3a. Care was taken when selecting the geometrical dimensions of the pin-hole configuration (diameter, length of pin hole) in order to ensure that the resonant frequency associated with the arrangement (similar to a Helmholtz resonator) was greater than 20 kHz, which is outside the range of interest. This was done by performing tests on a flat plate with microphones under different pin-hole geometrical configurations. The dimensions of the microphone and final pin-hole configuration are indicated in Fig. 3c.

To be able to measure the surface-pressure fluctuations very close to the TE, additional microphones were located inside the airfoil far from the pin hole, since due to the reduced space close to the TE, they could not be placed directly beneath the pin hole. They were linked to the pin holes on the surface by plastic tubes. An illustration showing this remote microphone arrangement can be seen in Fig. 3b. The plastic tubes of 0.4 mm internal diameter run along inner passages and were continued "infinitely" to avoid reflections from standing waves. They were made to pass through boxes that contained the microphones on one of their lateral sides. The pressure fluctuations were felt by the microphones through a small hole in the wall of the plastic tube. With this method, in the blunt TE model, it was possible to measure the pressure fluctuations as close to the edge as 2 mm (1% of the chord), less than 1 δ^*_{TE}.

C. Outline of Surface Microphone Arrays

In Fig. 4 the surface microphone array is indicated. The positions of the pin holes on the surface are summarized in Table 1. Note that the black dots in the figure represent the location of the pin holes but do not correspond to their actual smaller size (0.4 mm). Also note that the position of the pin holes correspond to the microphone physical location for those microphones in the pin-hole configuration, but the microphones in the remote microphone arrangement are placed further inside the airfoil.

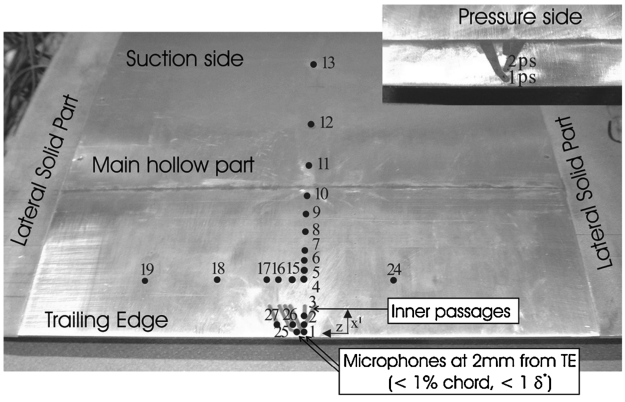

Fig. 4 Surface microphone array. The system of coordinates indicated (x', z) has its origin at the TE and at the airfoil midspan, but it is shown displaced to allow the visualization of the location of the pin holes where the surface-pressure fluctuations were measured near the TE.

Table 1 Positions of microphones in the airfoil model

Microphone number	x/C[a]	Distance from TE[b], x', mm	Distance from midspan, z, mm
1[c], 25[c]	0.99	2.0	0, 2
2[c], 26[c], 27[c]	0.98	5.0	0, 4, 10
3[c]	0.97	10.0	0
4, 15, 16, 17, 18, 19, 24	0.92	25.0	0, 5, 10, 15, 35, 65, −35
5	0.90	30.0	0
6	0.88	35.0	0
7	0.86	40.0	0
8	0.83	50.0	0
9	0.80	60.0	0
10	0.76	70.0	0
11	0.70	89.2	0
12	0.61	117.2	0
13	0.42	173.2	0
14	0.16	250.0	0
1ps[c]	0.99	2.0	0
2ps[c]	0.98	5.0	0
8ps	0.83	50.0	0

[a]Chordwise distance from the LE to the microphone location (to the pin hole), normalized by the chord of the airfoil ($C = 297$ mm).
[b]Chordwise distance from the TE to the microphone location (to the pin hole).
[c]Microphones placed using the remote microphone arrangement illustrated in Fig. 3b.

D. Measurement Techniques

The different measurement techniques used in the investigation are summarized next.

1. *Steady-Pressure Measurements*

The surface static pressures were measured with conventional static-pressure tappings. These were holes drilled normal to the airfoil surface with a diameter of $\simeq 0.3$ mm. They were located at a different spanwise location than that of the unsteady-pressure measurements (midcenterline) not to interfere with the microphone instrumentation. The pressure tappings were connected to a Scanivalve multiplexer that had a Druck PDCR 22 pressure transducer with 37 mbar g range. The calibration of the pressure transducer was performed using a DPI520 pressure indicator. The slope of the linear calibration was used. The random error of the Scanivalve multiplexer is ±2 Pa. The Scanivalve allows measurements of different static tappings (up to 50) with the same pressure transducer.

The inlet flow conditions to the test section were measured by means of static tappings on the side walls and a total pressure probe (inlet diameter of head $\simeq 1.3$ mm) in the freestream. These inlet conditions were measured at a distance of 0.3 times the chord of the airfoil upstream of the leading edge and of 0.25 times the chord below the airfoil midcenterline. At the outlet, the static tappings employed to monitor the flow conditions were placed on the side walls above the TE at a distance of 0.3 times the chord. These pressures were measured with the DSA 3017, with a random error of ±1.25 Pa. Note that the inlet velocity seemed to be affected by the airfoil potential field, as it was confirmed by numerical steady Reynolds-averaged Navier–Stokes simulations, resulting in a value of ≈2% lower than the outlet velocity. Therefore, the freestream velocity measured at the outlet has been used to normalize the data (e.g., the boundary-layer mean velocity and turbulence intensity profiles).

The static-pressure distribution of a blade is defined by means of the pressure coefficient or non dimensional isentropic velocity distribution:

$$Cp = \frac{P_{01} - p_s}{P_{01} - p_{s2}} = \left(\frac{V_x}{V_{2_{\mathrm{is}}}}\right)^2 \tag{1}$$

where P_{01} is the inlet total pressure, p_s is the surface static pressure and p_{s2} is the exit static pressure. $P_{01} - p_{s2}$ is the isentropic exit dynamic head.

2. *Unsteady-Pressure Measurements*

The microphones used in the investigation are FG-3329-P07 microphones from Knowles Electronics with a diameter of 2.5 mm and a height also of 2.5 mm with a sensing area of about 0.8 mm. They have been presented earlier in this section in Fig. 3. The sensitivity of the FG-3329-P07 microphone was provided by the manufacturer to be about 22.4 mV/Pa (45 Pa/V) in the flat region of the microphone response (from 70 to 10,000 Hz approximately). From the calibrations performed in the laboratory, the sensitivity of the FG-3329-P07 microphones employed varied approximately between 20.2 mV/Pa and 23.5 mV/Pa. The microphones were powered by two units with eight channels each, containing the circuits needed for each microphone. The microphone signals were amplified and low-pass-filtered at 30 kHz before being connected to the BNC-2090 connector panel. The microphone power units and the amplifier/filter units were designed and manufactured by the Electronics Development Group at the Engineering Department of the University of Cambridge.

The fast-response pressure transducer used in the calibration of the microphones was an Endevco FG-3329-P07. This transducer had a range of 1 psi, which was equivalent to 200 mV, according to specification. Since the maxima in the pressure fluctuations were of the order of a couple decades of Pa, a gain of 700 was used. The Endevco transducer had a diameter of $\approx$2.5 mm (2.34 mm). An Endevco Model 136 dc Amplifier was used to amplify and power the transducer with an input voltage of 10 V dc. The calibration was performed using the DPI520 as a pressure source. The response of the Endevco transducer (Pa versus V) was linear, with a sensitivity of approximately 115 Pa/V. The random error of the Endevco system (including the pressure transducer and the signal conditioner) is $\pm$0.09 Pa.

To calibrate the microphones, the output from a white noise signal generator was connected to a loudspeaker that was placed at one end of a tube. At the other end, in a cap closing the tube, the FG-3329-P07 and the Endevco were placed equidistant from the center of the circular cap. The FG-3329-P07 was placed under a pin-hole configuration with the same dimensions as the one on the airfoil and the Endevco was flush-mounted. The Endevco known calibration is constant with frequency for the range of frequencies of interest, i.e., up to 20 kHz. This method of calibration is based on the calibration procedure from Mish [34].

For the microphones connected to pin holes very close to the TE, and hence placed inside the airfoil using the remote arrangement, the calibration was done by placing the calibration tube (left open at the opposite end of the loudspeaker) upside down covering the pin holes of the microphones to be calibrated. At the same time, it covered an Endevco flush-mounted on a small flat plate temporarily connected to the TE of the airfoil.

The microphone data measured in order to characterize the wall-pressure field were acquired with a sampling frequency of 65,536 Hz and a total of $2^{23} = 8,388,608$ samples were recorded. The uncertainty in the surface-pressure spectra is mainly due to the statistical convergence error, which is inversely proportional to the number of records used. To reduce the statistical convergence error, the spectra have been calculated as the average of the spectra of individual data records obtained from dividing the pressure time series into a sequence of records. The total number of records used was 1024 resulting in an uncertainty of about 3% (where $1/\sqrt{N_r}$ and N_r are the number of records).

3. *Hot-Wire Anemometry*

Constant temperature hot-wire anemometry single and cross-wire probes has also been used in the present investigation in order to measure the velocity field.

The hot-wire instrumentation included a fully integrated constant temperature anemometer with built-in signal conditioning. The ac and dc components were logged separately using different preamplifier gains in order to ensure the adequate resolution of the fluctuating ac component. This component was obtained by bandpass-filtering the signal between 1 Hz and 30 kHz. The signal was then reconstructed by adding the dc level to the zero-mean filtered ac output and thereby enhancing the signal resolution.

The single-hot-wire Dantec-type P15 boundary-layer probe had a tungsten element of 1.2 mm length and 5 μm diameter set to an overheat ratio of 1.8. A Dantec 56C01 constant temperature anemometer was used in conjunction with a Dantec 56C17 bridge and a Dantec 55N22 signal conditioning unit. A logging frequency of 65,536 Hz, equal to the sampling frequency of the microphones, was used. For the mean and rms profiles, a total of $2^{19} = 524,288$ samples for the ac signal and of $2^{17} = 131,072$ samples for the dc signal were acquired. When acquiring simultaneously velocity and surface-pressure data, $2^{20} = 1,048,576$ samples were acquired at each channel of the data-acquisition board, and to calculate the cross-correlation between velocity and pressure, a total of 256 records were used.

The hot-wire probe was calibrated in the freestream region of the test section by logging the voltage from the probe together with the total and static pressures from a pitot-static probe. The two plates were at approximately the same streamwise position and at slightly different spanwise positions so that the measurements did not interfere. A best-fit calibration for King's law was then obtained.

The surface of the airfoil was detected by using a resistance circuit that measured the electrical contact between the probe and the surface. The effect of air temperature drift has been taken into account with the correction described by Bearman [35] and in order to take into account the proximity of the surface and its effect on the cooling of the wire, a traverse with no flow was performed to find out the Cox [36] correction to be applied to the measured data.

The cross-wire probe that was used to simultaneously measure the normal and streamwise components of velocity, at the same time as the surface pressure, was a subminiature boundary-layer probe, especially designed by Dantec to given specifications. The length of the wires was 0.7 mm with a diameter of 2.5 μm. The angle between each wire and the horizontal axis is 45° and the angle between the wires is 90°. This subminiature cross wire enabled measurements as close to the surface of the airfoil as 0.3 mm, which is approximately 3% of the boundary-layer thickness δ, at the TE (or 15% of the displacement thickness, δ^*) for these separated laminar boundary-layer cases.

A yaw calibration was performed in a calibration nozzle to determine the relationship between the effective cooling velocity for each wire and the velocity components u and v and to confirm the angle between the two wires of the cross-wire configuration. The form of the yaw-response function used in the present study is that proposed by Champagne et al. [37] and Champagne and Sleicher [38].

The velocity with the cross-wire probe was measured at approximately 80 wall-normal (y) locations. These locations went from $y = 0.3$ to 40 mm. The increments were approximately of 0.05 mm up to 0.1δ, 0.1 mm up to 0.2δ, 0.5 mm up to δ, 1 mm up to 1.5δ and 5 mm up to at least 2δ. When the cross wire was traversed in the wake of the airfoil, i.e., downstream of the TE, those y locations where measured above and below the airfoil midcenterline and extra locations were added between $y = 0.3$ and -0.3 mm at intervals of 0.05 mm (0 mm corresponds to the cross wire behind the TE on the virtual airfoil midcenterline).

4. *Oil and Dye Flow Visualization*

A conventional oil and dye flow visualization technique was used in this study. Diesel oil was mixed with a dye to form a uniform mixture that was then applied to the surface of the airfoil. For the low Reynolds number, i.e., $Re_c = 2 \times 10^5$, apart from a mixture of diesel oil and dye, another mixture of paraffin oil and dye was used leading to better results in this case. The wind tunnel was run at the corresponding flow conditions for at least 30 min, allowing the flow pattern to develop. For both Re_c investigated, different oil/dye ratios were tested.

III. Results

A. Static-Pressure Results

The static-pressure distribution is defined by means of the pressure coefficient C_p, defined in Eq. (1). Because of the reduced space very near the trailing edge, it was not possible to have static tappings very close to the edge; therefore, static-pressure data are not presented in that region.

In Fig. 5, the static-pressure distribution along the NACA0012 airfoil is illustrated for the two Re_c investigated at 0° AOA. The distribution under tripped and untripped boundary layers has been represented in the same plot, together with the result from the inviscid flow calculation. Note that the tripped boundary layers were obtained by placing a trip wire at 12.7% of the chord from the leading edge, on both sides of the airfoil. This resulted in a turbulent boundary layer (TBL). In Fig. 5a, the static-pressure distribution for $Re_c = 4 \times 10^5$ is shown. It can be observed that the experimental data corresponding to the untripped boundary layer deviate from the data associated with the tripped boundary layer in the region approximately between $x/C = 0.7$ and 0.85. This indicates that the flow is separating in that region and reattaching afterward creating a separation bubble.

In Fig. 5b, the static-pressure distribution for $Re_c = 2 \times 10^5$ is displayed. As in the high-Re_c case without trip wire, the experimental data deviate from the trip-wire distribution and, therefore, from the inviscid flow calculation. In this case, the deviation is more pronounced than in the $Re_c = 4 \times 10^5$ case and it occurs for a larger region, from approximately $x/C = 0.65$ to $x/C > 0.9$. The separation bubble is larger in this case and the flow reattaches further downstream, immediately upstream of the TE.

B. Boundary-Layer Integral Parameters

Because of the streamline curvature, the freestream velocity over the airfoil varies in the surface normal direction. Therefore, in order to calculate the boundary-layer thickness δ, a polynomial of 2nd order was fitted to the points that were outside the boundary layer up to a distance normal to the wall of at least 5δ. The boundary-layer thickness was defined at the point where the velocity was 99.5% of the velocity of the traverse position (y) where the fitting polynomial deviated from the boundary-layer profile. The velocity at this point was defined as U_e, velocity of the edge of the boundary layer. This has been illustrated in Garcia-Sagrado and Hynes [39].

In Fig. 6 and Table 2, the integral parameters and shape factor H_{12} at different streamwise locations upstream and downstream (wake) of the TE (downstream positions only indicated in the table) are presented for the two Re_c investigated. Note that in Fig. 6, the integral parameters from a tripped boundary layer on the NACA0012 airfoil at 0° AOA (TBL) have also been presented for comparison.

For both Re_c, the boundary layer is laminar up to the point where it separates, due to the adverse pressure gradient (APG), then it undergoes transition along the separated shear layer and reattaches upstream of the TE. The transition occurs earlier for the high Re_c and so does the reattachment of the separated shear layer, resulting in a shorter separation bubble than for the low Re_c.

From the analysis of the velocity profiles (and contour plots) and an oil and dye flow visualization (presented in the next sections) together with the static-pressure distribution and the evolution of the integral parameters, it has been possible to determine the approximate location of the separation point x_s, the maximum displacement of the separated shear layer x_{MD}, and the reattachment point x_R. The determination of the onset of transition has been done by careful analysis of the temporal signals of velocity (hot-wire and cross-wire probes) and pressure (surface microphone array) and their spectra. Furthermore, the correlations proposed by Hatman and Wang [1] to determine separated-flow main parameters have also been considered, although with caution, since they were developed from flat-plate data, but limited airfoil data.

In Figs. 6b and 6d, the displacement thickness δ^* and shape factor H_{12} from the untripped boundary-layer cases can be seen to increase significantly up to a maximum value and decrease afterward toward the TE. The value of H_{12} upstream from separation at $x/C = 0.4$ (Fig. 6d), approximately 2.1 and 2.6 for the high and low Re_c, respectively, is typical of a laminar boundary layer (Schlichting [40]). This value increases toward the separation point, reaching a value of 2.8 and 3.25 at separation for $Re_c = 4 \times 10^5$ and $Re_c = 2 \times 10^5$, respectively. A typical value of H_{12} at separation in a laminar boundary layer is approximately 3.5 (Young [41]), although similar to the present study, evidence of separation at lower values has been found in the literature (Lang et al. [42]). The separation point x_s has been estimated to be at approximately $x/C = 0.65$ for $Re_c = 2 \times 10^5$ and $x/C = 0.73$ for $Re_c = 4 \times 10^5$. These values also correspond to a Pohlhausen pressure-gradient parameter $\Lambda_\theta = \frac{\theta^2}{\nu}\frac{\mathrm{d}U_\infty}{\mathrm{d}x}$ of -0.082, which is the empirical value of this parameter that Thwaites [43] suggested at separation. Similarly to the observations from Volino [44] and Lin and Pauley [45], as Re_c increases the separation point moves downstream and the reattachment location moves upstream, resulting in a shortened time-averaged separation bubble. Lin and Pauley [45] also reported a reduced separation angle

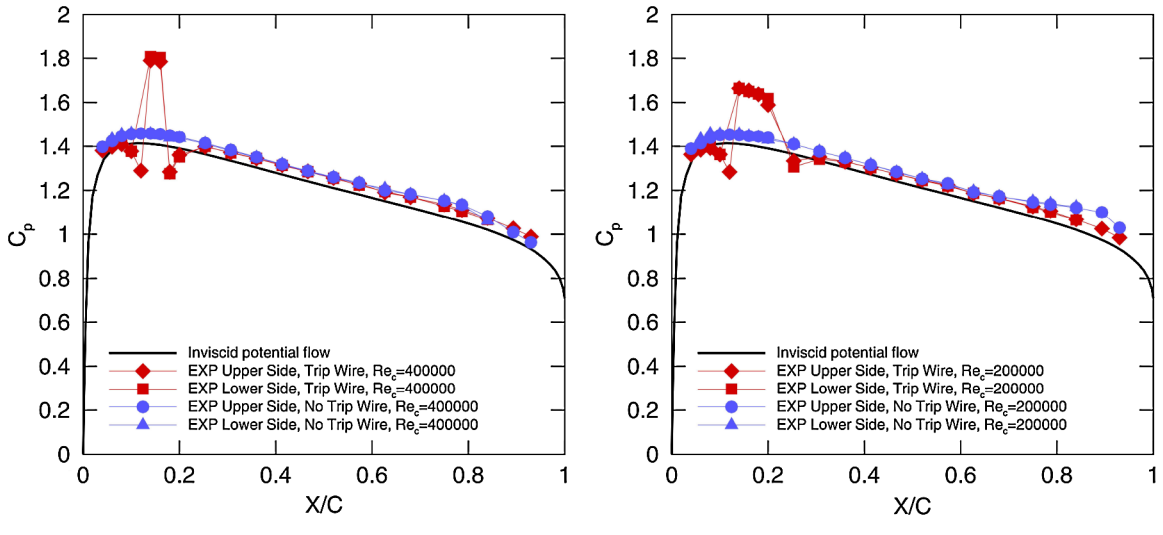

a) b)

Fig. 5 Static-pressure distribution for the two Reynolds numbers investigated. Results from a tripped boundary layer (trip wire) have also been presented for comparison with the untripped boundary-layer results: a) $Re_c = 4 \times 10^5$ and b) $Re_c = 2 \times 10^5$.

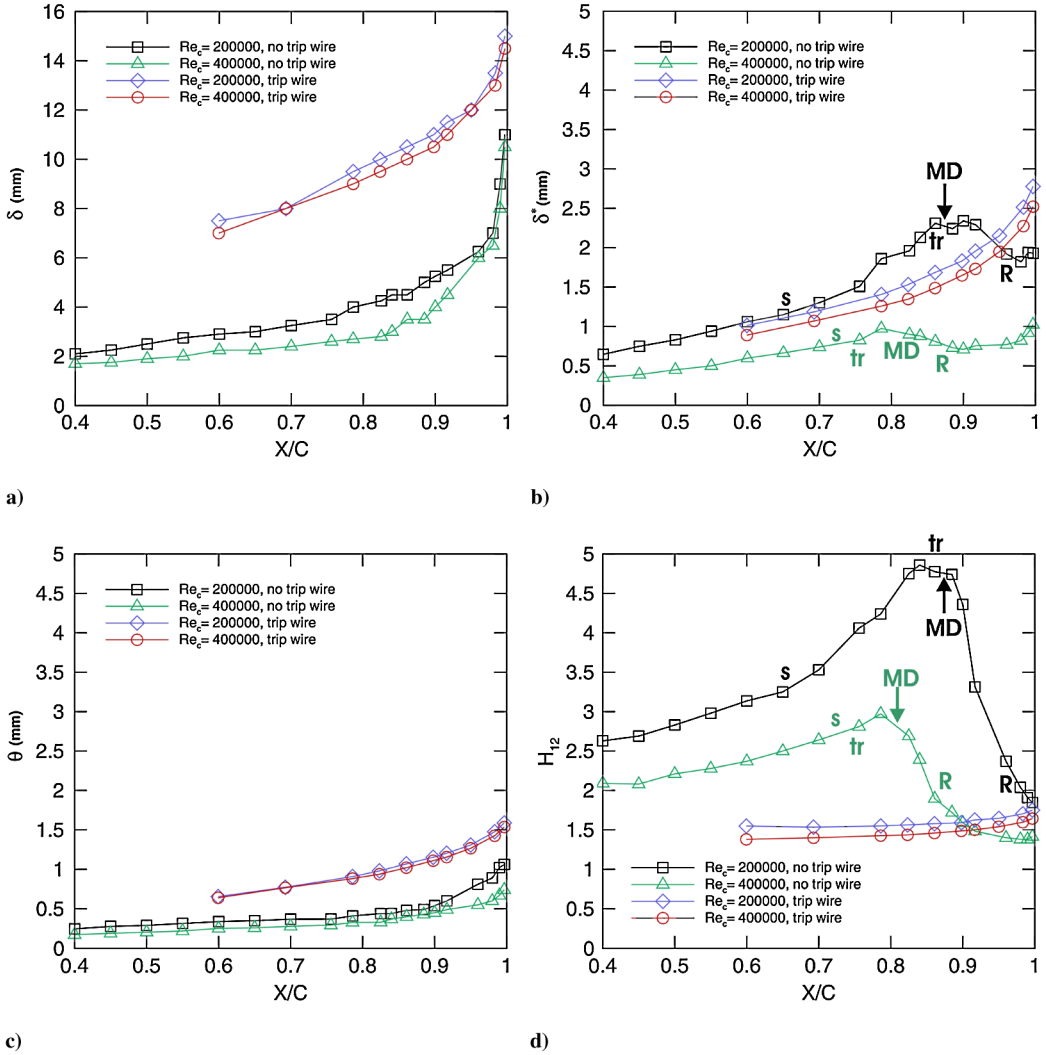

Fig. 6 Boundary-layer integral parameters for the two Reynolds numbers investigated. Comparison between tripped (TBL) and untripped boundary-layer (separated BL) results. The locations of the separation (*s*), onset of transition (tr), maximum displacement (MD), and reattachment (R) points are indicated in the figure. These locations have also been summarized in Table 3.

as the Re_c increased. The previous observations can be visualized in the contour plots in the next section.

As Hatman and Wang [46] reported, δ^* and H_{12} reach a maximum in the region around the maximum displacement of the separated shear layer, x_{MD}. From Figs. 6b and 6d, it can be seen that x_{MD}/C is approximately 0.86 to 0.88 for $Re_c = 2 \times 10^5$ and 0.82 or 0.83 for $Re_c = 4 \times 10^5$. It can also be seen in Fig. 6a that the initial growth rate of the shear layer up to x_{MD} is significantly lower than that downstream of x_{MD}. Hatman and Wang [47] indicated that the rapid growth of the boundary-layer thickness δ between x_{MD} and x_R was related to the periodic ejection of fluid from the separated region into the shear layer. They also reported that after reattachment, even if the resulting TBL is structurally different from the one resulting from transition in an attached flow, H_{12} decreased to a value very close to the value under a TBL ($\approx$1.4). In the higher Re_c case under the untripped boundary layer, it can be seen in Fig. 6d that indeed H_{12} after reattachment is about 1.4. In the lower Re_c case, H_{12} at the TE is about 1.8, due to the fact that the reattachment point x_R for this Re_c

Table 2 Integral parameters for both Re_c investigated (2×10^5 and 4×10^5)[a]

Distance to TE, mm, x/C	δ, mm	δ^*, mm	θ, mm	H_{12}	U_e, m/s	$U_{\infty,i}$, m/s	$U_{\infty,o}$, m/s
177, 0.404	2.10, 1.70	0.65, 0.35	0.25, 0.17	2.63, 2.01	11.17, 21.62	10.10, 20.00	10.33, 20.47
102, 0.656	3.00, 2.25	1.15, 0.66	0.35, 0.26	3.25, 2.50	11.50, 21.83	10.67, 20.90	10.90, 21.30
70, 0.764	3.50, 2.60	1.51, 0.83	0.37, 0.30	4.06, 2.81	11.24, 21.82	10.68, 21.20	10.87, 21.55
52, 0.825	4.25, 2.80	2.02, 0.90	0.43, 0.33	4.70, 2.70	11.07, 21.16	10.52, 21.03	10.71, 21.38
42, 0.860	4.50, 3.50	2.31, 0.81	0.48, 0.43	4.78, 1.90	10.04, 19.90	9.89, 19.60	10.09, 20.00
27.5, 0.900	5.25, 4.00	2.34, 0.71	0.54, 0.45	4.36, 1.59	10.86, 20.18	10.38, 20.89	10.55, 21.24
12, 0.960	6.25, 6.00	1.92, 0.77	0.81, 0.55	2.37, 1.40	10.52, 19.30	10.65, 20.56	10.85, 20.90
5, 0.983	7.00, 6.50	1.82, 0.82	0.89, 0.60	2.04, 1.38	10.15, 19.45	10.68, 21.17	10.85, 21.53
2, 0.993	9.00, 8.00	1.94, 0.92	1.02, 0.67	1.91, 1.38	9.71, 19.17	10.27, 20.81	10.43, 21.14
1, 0.997	11.00, 10.50	1.93, 1.02	1.06, 0.74	1.82, 1.38	10.26, 19.48	10.80, 21.14	10.98, 21.47
−2, 1.010	13.00, 12.00	2.59, 1.59	1.27, 0.92	2.03, 1.73	9.37, 18.00	9.91, 19.14	10.07, 19.43

[a] The first number before the comma corresponds to the lower Re_c, and the number after the comma corresponds to the higher Re_c.

lies very close to the TE, somewhere between $x/C = 0.93$ and $x/C = 0.96$, and the attached boundary layer does not have time to reach $H_{12} \approx 1.4$ before the edge.

From the temporal signals of velocity and surface pressure and their spectral behavior (only surface-pressure spectra has been included in this paper for conciseness; see Sec. III.E), the onset of transition x_{tr} was determined to be between x_s and x_{MD} for both Re_c. This point was defined as the location where the instability waves that became amplified along the separated shear layer, yielded to the appearance of a broader range of selected frequencies. For $Re_c = 4 \times 10^5$, x_{tr} seems to be approximately at $x/C = 0.75$ close to x_s, and for $Re_c = 2 \times 10^5$, x_{tr} seems to be at approximately the location of x_{MD}, between $x/C = 0.86$ and $x/C = 0.90$. Hatman and Wang [47] pointed out that during transition, there is a significant change in the boundary-layer integral parameters and that the process of transition involves an increase in the momentum thickness θ and a decrease in H_{12}. This can be seen in Figs. 6c and 6d. In Table 3 the main parameters that characterized the separated boundary layers are summarized.

Transition can be influenced by different parameters such as pressure gradients, freestream turbulence intensity, acoustic waves, surface vibration, surface curvature, surface roughness, etc. It can also be affected by an acoustic-feedback mechanism where the acoustic waves at the TE propagate upstream to some location of receptivity and generate further instability waves within the boundary layer (Sandberg et al. [19] and Jones et al. [20]). These parameters and mechanisms can affect the start and length of the transition and the structure of the transitional boundary layer. Mayle [48] classified the modes of transition in a boundary layer as natural transition, bypass transition, separated-flow transition, periodic-unsteady transition, which is also called wake-induced transition, and reverse transition. Under low freestream turbulence intensity and zero-pressure-gradient conditions, natural transition is expected. Here, the boundary layer becomes unstable to small disturbances, which begin to grow as Tollmien–Schlichting (T-S) waves. Through amplification of the T-S waves and nonlinear vorticity breakdowns, the flow becomes turbulent. Under high freestream turbulence intensity or surface roughness, large disturbances can cause bypass of the linear growth stages of transition and hence of the T-S mode of instability, resulting in the sudden appearance of turbulent spots. The reverse transition refers to the transition from turbulent to laminar and is also called *relaminarization*. It occurs when the acceleration (favorable pressure gradient) on the pressure side of the airfoil is strong enough.

In large APGs or mild gradients with low Reynolds numbers, a transitional separation bubble occurs. The separated shear layer is inherently unstable and results in the growth of disturbances that yield to an earlier transition. Turbulent mixing due to the increased entrainment in the fast growing turbulent part of the shear layer causes the layer to reattach. With an increase in the APG or reduction in the Reynolds number, the separated shear layer may not reattach and the bubble bursts to form a long bubble or an unattached free shear layer.

When a separation of the boundary layer takes place, the flow becomes detached from the surface, allowing a region of reverse flow to develop between the surface and the separated shear layer. This is illustrated in Fig. 7 (illustration based on Mayle [48]).

The transition to turbulence in separated boundary layers has been reported to be the result of the superposition of the effects of two different types of instabilities (Hatman and Wang [1,49], Volino [44], Roberts and Yaras [50], and Lou and Hourmouziadis [51]). The first type of instability is the Kelvin–Helmholtz (K-H) instability, which is associated with the separated laminar shear layer, and the second type

Table 3 Main parameters characteristic of the separated flow on the NACA0012 airfoil for both Re_c investigated

	x_s/C	x_{tr}/C	x_{MD}/C	x_R/C
$Re_c = 2 \times 10^5$	0.65	0.86 to 0.90	0.86 to 0.88	0.93 to 0.96
$Re_c = 4 \times 10^5$	0.73	0.75	0.82 or 0.83	0.85 or 0.86

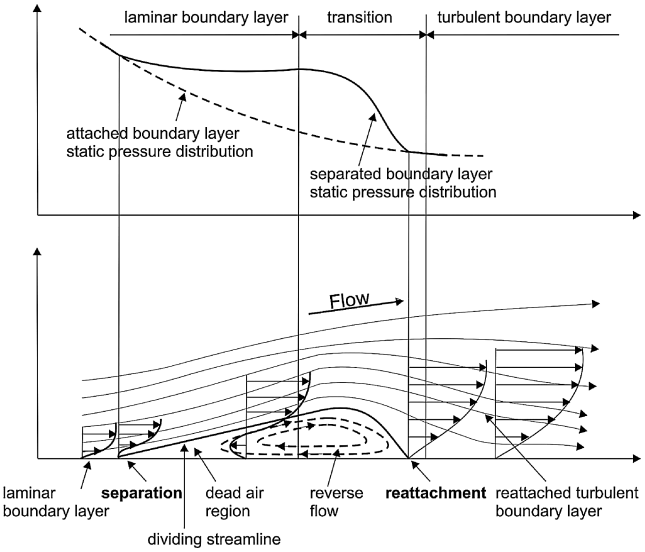

Fig. 7 Schematic of a separated laminar boundary layer.

of instability is the convective T-S instability, which is normally originated upstream of the separation point and it evolves and interacts with the K-H instability along the separated shear layer.

According to Hatman and Wang [46], separated boundary layers that separate in a laminar state behave differently from those that are transitional or highly unstable (pretransitional) at separation. In general lines, they defined a *laminar separation bubble* to be when separation started in the laminar flow and a *transitional separation bubble* to be when separation happened downstream of the onset of transition. This classification is rather general, given the complexity of the separated-flow-transition mechanism, and Hatman and Wang [46] also indicated a succession of intermediate stages dominated by one mode of transition or another. In the current case, the separated flow at $Re_c = 4 \times 10^5$ has been identified with the laminar-separation/dominant-transitional-separation mode and the separated flow at $Re_c = 2 \times 10^5$, with the laminar-separation short-bubble mode or laminar-separation forced-short-bubble mode. This has been done after identifying structures and flow behavior similar to those described by Hatman and Wang [46] for these modes.

In both cases, the onset of transition x_{tr} happens downstream of the separation point x_s. However, at $Re_c = 4 \times 10^5$ it occurs close to x_s, with the separation point most likely in a pretransitional state, whereas at $Re_c = 2 \times 10^5$, it takes place further downstream of x_s, in the region of the maximum displacement x_{MD}. At $Re_c = 4 \times 10^5$, T-S waves have been observed shortly upstream x_s that evolved and were amplified along the separated shear layer. Comparing the spectra of the temporal traces with those presented by Hatman and Wang [47] for the transitional separation mode, a similar hump has been observed at this Reynolds number. The hump can be seen in the wall-pressure fluctuations spectra in Sec. III.E. Similarly to them, the highest peak within the hump has been related to the T-S instability waves that in this case are the dominant mechanism in initiating the onset of transition. These T-S waves are influenced though by the K-H instability mechanism downstream of x_s and the hump is a result of the interaction between the two instabilities. They also pointed out that this mode is often accompanied by vortex shedding from the separated shear layer, and in the present results, a quasi-periodic vortex shedding was observed downstream of the reattachment point in the cross-correlation between pressure and velocity. The frequency of the vortex shedding has also been related here to the T-S waves.

At $Re_c = 2 \times 10^5$, the onset of transition happens in the region of x_{MD} and T-S waves have also been observed here close to x_s that were also amplified along the separated shear layer. The spectra of the temporal traces in this case, showed very distinctive peaks as it can be seen in Sec. III.E in the wall-pressure fluctuations spectra. These peaks were associated with periodic vortex shedding from the separated shear layer that remained a dominant feature in the

reattached TBL. The frequency of the vortex shedding has also been related to the T-S waves in this case.

C. Boundary-Layer Mean Velocity and Turbulence Intensity Profiles

Velocity profiles are presented next. Note that the directional insensitivity of hot-wire anemometry (employed in the measurements of the boundary-layer profiles) causes the velocity profiles to become distorted, particularly near the wall. This has been illustrated in Fig. 8 (illustration based on Hatman and Wang [46]).

In Fig. 9 the mean velocity and turbulence intensity profiles at different streamwise positions upstream, within, and downstream of the separation bubble up to the TE are presented for the two Re_c. It can be seen that the separation bubble is larger for the low Re_c, with the boundary-layer profiles easier to characterize than for the high-Re_c scenario, especially close to the wall. For both Re_c, the profiles after the separation point show an inflexion point in the near-wall region and look attached after the reattachment point, transitioning toward the shape of profiles under a turbulent boundary layer as they moved downstream of the reattachment region.

For the low Re_c (Fig. 9a), it can be seen that separation starts at $\approx x/C = 0.65$ with the mean boundary-layer profile at this location showing an inflexion point near the wall (Fig. 9a, top left). By $x/C = 0.78$ and $x/C = 0.82$ the boundary layer (BL) is fully separated with a well-defined inflexion point. In the profiles at $x/C = 0.86$ to $x/C = 0.92$ (Fig. 9a, top right), it is possible to observe the distortion of the boundary-layer profile mentioned above, indicating a strong recirculating region. The mean velocity profiles at $x/C = 0.98$ and $x/C = 0.99$, show a reattached boundary layer. In the turbulence intensity profiles (Fig. 9a, bottom), it is seen how when the boundary layer is not yet separated or shortly after separation (Fig. 9a, bottom left), the level of velocity fluctuations u' is very low. As the separated BL approaches transition at $x/C = 0.86$ or $x/C = 0.88$, the levels increase and continue to increase as the separated BL becomes turbulent from $x/C = 0.90$ onward. At reattachment, near $x/C = 0.96$ and shortly afterward the levels are the highest.

For the high Re_c (Fig. 9b), the boundary layer separates later, between $x/C = 0.70$ and $x/C = 0.75$ (Fig. 9b, top left) and since it is a smaller separation bubble that stays closer to the wall, the inflexion point is less evident. Observing the shape of the profiles, it can be noted that the separated BL reattaches between $x/C = 0.84$ and $x/C = 0.86$ (Fig. 9b, top right). The profiles from $x/C = 0.88$ onward start looking like typical turbulent boundary-layer profiles (Schlichting [40]). Figure 9b (bottom) show the turbulence intensity profiles, and as in the low-Re_c case, the level of fluctuations increase dramatically after transition at $x/C = 0.75$, reaching maximum values around reattachment from $x/C = 0.86$ to $x/C = 0.88$ (Fig. 9b, bottom right). From $x/C = 0.98$ and $x/C = 0.99$, typical turbulence intensity profiles can be seen near the TE.

Another illustration of the shape of the bubble can be seen in the contour plots of streamwise mean velocity in Figs. 10a and 10c. In Fig. 10a, it can be seen that indeed the BL separates at $\approx x/C = 0.65$ and reattaches somewhere between $x/C = 0.93$ and $x/C = 0.96$. The turbulence intensity levels in Fig. 10b can be seen to increase considerably toward reattachment and afterward, as the boundary layer becomes turbulent. In Fig. 10c, it can be corroborated that for the high Re_c the separation bubble is smaller and closer to the wall, it separates later and reattaches earlier ($x/C = 0.73$ and 0.86, respectively). Again the level of fluctuations can be observed to increase significantly toward the reattachment region (Fig. 10d).

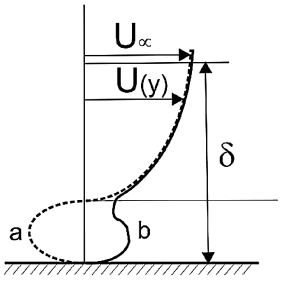

Fig. 8 Separated boundary-layer profile distortion by hot-wire measurements. The distorted profile is b.

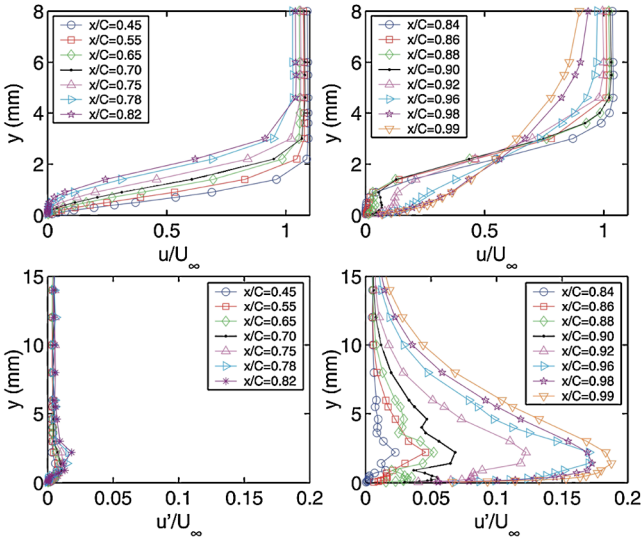

a)

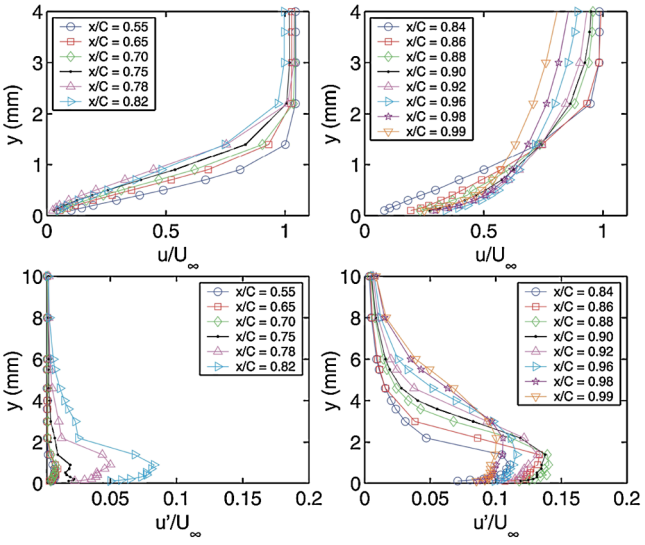

b)

Fig. 9 Boundary-layer mean velocity and turbulence intensity profiles at different streamwise positions over the NACA0012 airfoil: a) $Re_c = 2 \times 10^5$ and b) $Re_c = 4 \times 10^5$.

D. Oil and Dye Flow Visualization

Figure 11a illustrates the oil and dye flow visualization performed at $Re_c = 4 \times 10^5$. A solution made of diesel oil and dye was used in the flow visualization. Different streamwise locations have been indicated on the left side of the figure as a reference. A dark area is observed on the visualization that has a U shape, due to the effect of the side walls supporting the airfoil. On the side walls, due to the boundary layer developing on them, a horseshoe vortex develops that grows in size with downstream distance. Focusing on the region far away from the side walls, around midspan, it can be seen that the dark area ends at about $x/C = 0.86$. This location coincides with the reattachment point of the separation bubble at this Re_c. The authors believe that the dark area is due to the recirculating region in the later part of the separation bubble upstream of the reattachment point. This recirculating flow moves the "paint" (dye and oil mixture) upstream in the first instants of the flow visualization but does not have the

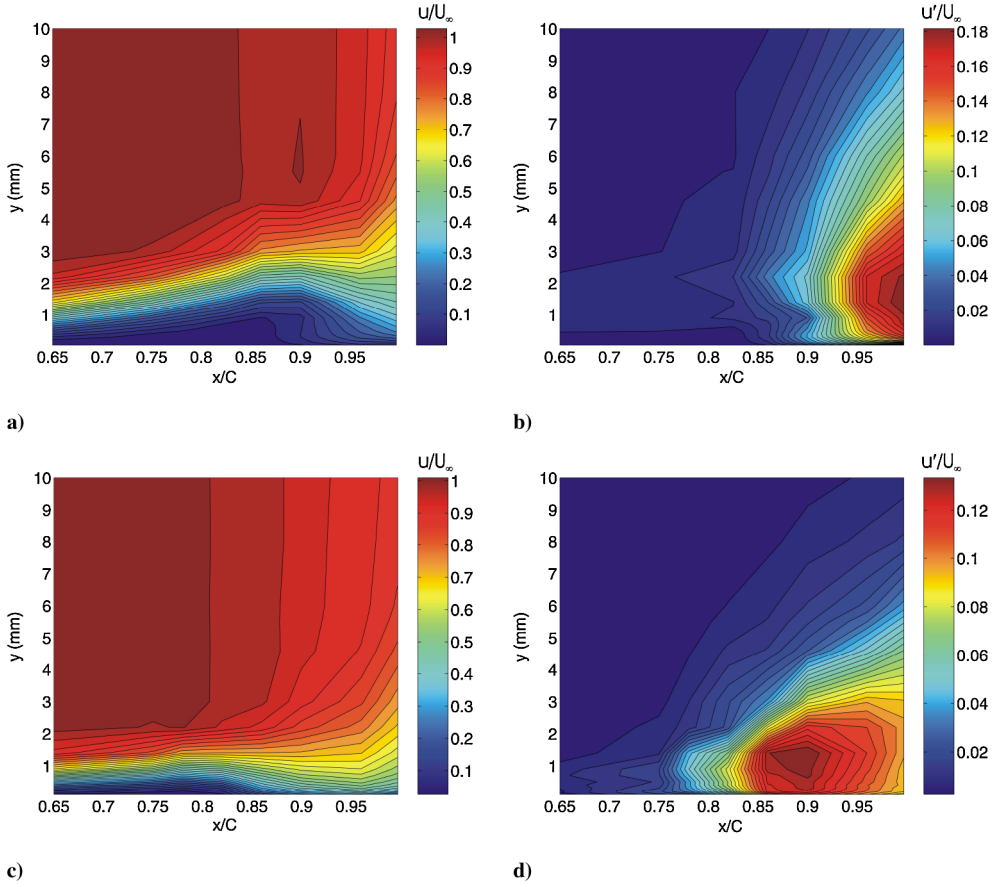

Fig. 10 Boundary-layer mean velocity and turbulence intensity contour plots over the NACA0012 airfoil: a–b) $Re_c = 2 \times 10^5$ and c–d) $Re_c = 4 \times 10^5$.

strength enough to recirculate it, i.e., to bring back the paint downstream. The separation point, which was found to be at about $x/C = 0.73$ from the velocity profiles, integral parameters, and the position where $\Lambda_\theta = -0.082$ (Thwaites [43]) cannot be easily observed on the flow visualization.

In Fig. 11b, the oil and dye flow visualization performed at $Re_c = 2 \times 10^5$ is presented. Because of the lower velocity (10 m/s against 20 m/s at $Re_c = 4 \times 10^5$), it was more difficult now to obtain a clear flow visualization, especially using the mixture of diesel oil and dye, despite trying with a combination of different mixtures (varying the concentration of dye). Hence, the visualization was also performed with a mixture of paraffin oil and dye, which is the picture that has been included here.

Again, a U-shaped dark region is observed, due to the boundary layers formed on the side walls as explained before. Similarly to the case at $Re_c = 4 \times 10^5$, the end of the dark region coincides approximately with the reattachment point, in this case, somewhere between $x/C = 0.93$ and 0.96. Therefore, it seems to corroborate that this dark region corresponds to the recirculating flow in the most downstream region of the separation bubble. Similarly to the previous case, the location of the separation point indicated earlier at $\approx x/C = 0.65$ is ambiguous from the visualization.

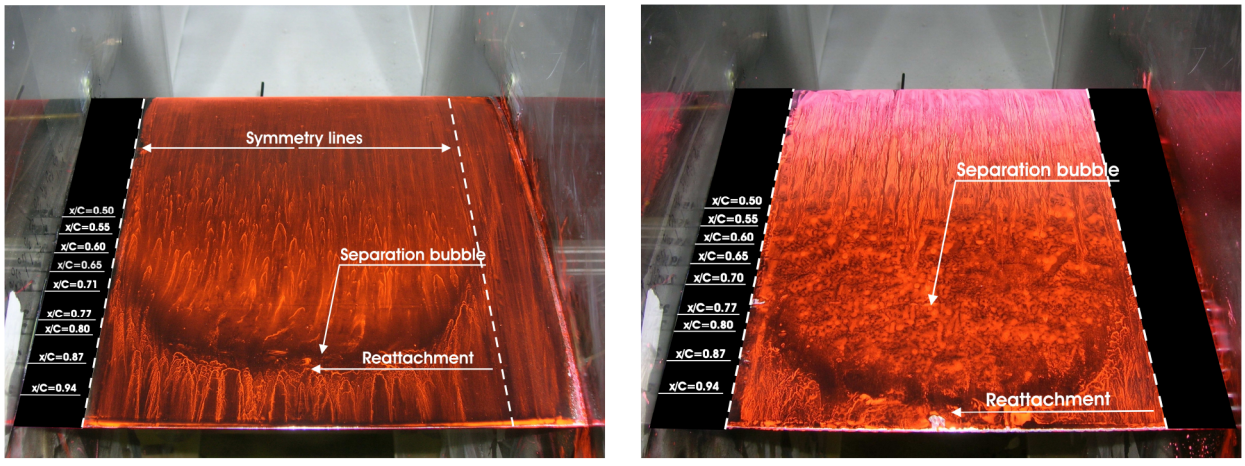

Fig. 11 Oil and dye flow visualization: a) $Re_c = 4 \times 10^5$ (diesel oil and dye flow visualization) and b) $Re_c = 2 \times 10^5$ (paraffin oil and dye flow visualization).

E. Wall-Pressure Power Spectra

Figure 12 illustrates the surface-pressure power spectral density at $Re_c = 2 \times 10^5$. At this Reynolds number, the laminar boundary layer separated in the second half of the airfoil, at approximately $x/C = 0.65$ ($x = 193$ mm), and reattached a short distance upstream of the TE, between $x/C = 0.93$ ($x = 279$ mm) and $x/C = 0.96$ ($x = 288$ mm). A main sharp peak can be seen at a frequency close to 200 Hz (approximately 190 Hz) at all microphones. This peak is related to the periodic vortical structures originated in the separated shear layer and is associated with the instabilities from the laminar boundary layer, the so-called T-S instability waves that become amplified along the separated shear layer, as described in Sec. III.B.

An expression from Stieger [52] following Walker [53] for the calculation of the frequency of the T-S waves is

$$f = \frac{3.2 U_\infty^2 Re_{\delta^*}^{-3/2}}{2\pi\nu} \tag{2}$$

where Re_{δ^*} is the Reynolds number based on the displacement thickness δ^* at the position where the instability waves are first observed in the pressure and velocity temporal signals.

With a δ^* at the position where the instability waves are first observed of approximately 1 mm, the frequency from Eq. (2) is 197 Hz, very close to the frequency of the main peak.

These disturbances interact with the K-H instabilities from the separated shear layer that could be related to the second peak ($\approx$230 Hz) in Fig. 12. The peaks in the spectra are part of a complex mechanism where the different instabilities interact. The peak close to 400 Hz, corresponds to the first harmonic of the fundamental peak.

Note that although the flow did not separate until about $x/C = 0.65$ and signs of the instability waves were not seen in the velocity signals as early as $x/C = 0.42$ or 0.61, the peaks can already be seen in the spectra of the microphones at those locations. This is due to the fact that in this case, the acoustic waves associated with these periodic disturbances propagate also upstream. This was confirmed in a wave-number/frequency spectrum, which has not been included in this paper, for brevity. This observation is in agreement with previous investigations on airfoils under a laminar boundary layer (Brooks et al. [54], Oerlemans and Migliore [55], Roger and Moreau [14], Desqesnes et al. [18], Sandberg et al. [19], and Jones et al. [20]) of an acoustic-feedback loop between the airfoil TE and an upstream location where the T-S waves originate. As the microphones approach the TE and after the transition takes place along the separated shear layer (at $\approx x/C = 0.86$ to 0.90), it can be seen that the energy content at high frequencies increases considerably. This is particularly the case after reattachment of the separated shear layer between $x/C = 0.93$ and $x/C = 0.96$, when the flow is highly transitional/turbulent. It can be observed that the main peak reaches a maximum value at the reattachment point and decreases afterward for the microphones closer to the TE, at $x/C = 0.98$ and 0.99. This is due to the interaction of the periodic disturbance with the smaller structures from the incipient TBL. Despite this, the disturbances associated with this tonal peak remain dominant in the flow.

In Fig. 13, the surface-pressure power spectral density for $Re_c = 4 \times 10^5$ is shown. For this Re_c, the boundary layer also separated in the second half of the airfoil, at approximately $x/C = 0.73$ ($x = 217$ mm), although in this case it reattached earlier, at approximately $x/C = 0.86$ ($x = 255$ mm). In the spectra of the microphones upstream of the separation, at $x/C = 0.42$ and 0.61, no particular structures can be identified and the flow remains laminar. At $x/C = 0.76$, a clear hump appears in the spectra, centered at around 600 or 700 Hz. Similarly to the scenario described previously, the hump seems to be due to the instabilities from the laminar boundary layer (T-S) that get amplified in the separated shear layer and interact with additional instabilities (K-H) from the separated region. Additional frequencies from a transitional state seem also present already at this location, since now the onset of transition is very close to the separation point. Hence, the nature of the disturbances is more broadband here than for the low Re_c and they have been referred to as quasi-periodic disturbances.

The hump increases downstream, also reaching a maximum value around the reattachment region ($x/c = 0.83$ to 0.90). Further downstream, it decreases considerably, due to the interaction of the quasi-periodic structures with a broader range of scales from the developing TBL. Nevertheless, the quasi-periodic disturbances shed from the separated shear layer, still have a significant presence in the flow.

A smaller hump can be seen in the spectra of the microphone closest to the edge ($x/C = 0.99$), at approximately 1400 Hz, which is associated with a quasi-periodic vortex shedding from the blunt TE. In the lower Re_c case in Fig. 12, there is no clear evidence of vortex shedding from the TE, which is most likely concealed by the stronger vortex shedding from the separated shear layer.

Evaluating expression (2), with a δ^* at the streamwise location where the T-S instability waves are first observed ($x/C = 0.65$) of approximately 0.66 mm, the frequency of the waves is found to be about 530 Hz. This frequency approximately coincides with the value at which the hump shows a maxima in the spectra.

Note that the acoustic-feedback mechanism described for the lower Re_c case is characteristic of tonal noise, i.e., when the structures present in the flow are very periodic in nature. Since in the case of the higher Re_c the structures present in the flow are more broadband in nature this mechanism is most likely weaker or not present.

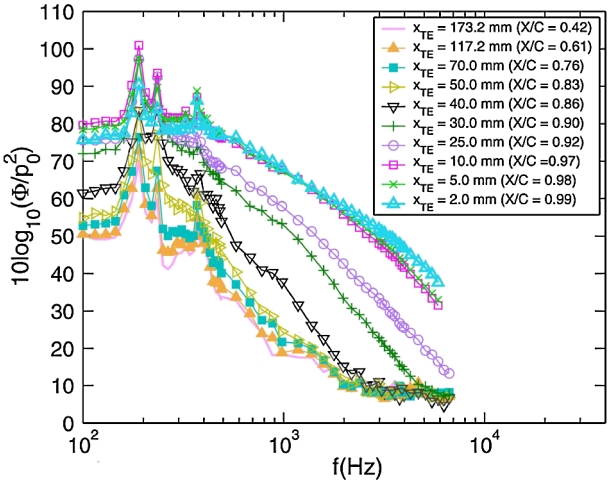

Fig. 12 Surface-pressure power spectral density referenced to $p_o = 20$ μPa at different streamwise locations on the NACA0012 airfoil and at $Re_c = 2 \times 10^5$.

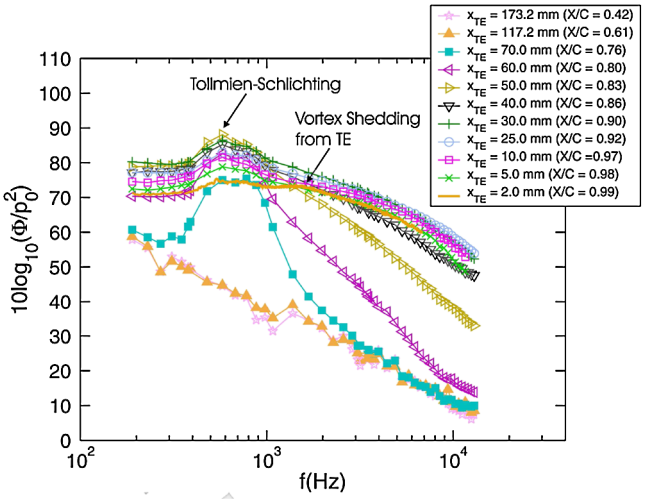

Fig. 13 Surface-pressure power spectral density referenced to $p_o = 20$ μPa at different streamwise locations on the NACA0012 airfoil and at $Re_c = 4 \times 10^5$.

F. Cross-Correlation Between Velocity and Surface Pressure

Cross-correlations between the velocity (streamwise and normal components) measured by a subminiature cross wire in the boundary layer and wake, and the pressure fluctuations from the microphones on the surface close to the TE are presented next. The temporal cross-correlation coefficients are calculated as

$$R_{up}(\tau, y) = \frac{\overline{u'(\xi_o, y, t+\tau)p'(\xi_m, t)}}{U_e p_{\text{rms}}} \tag{3}$$

$$R_{vp}(\tau, y) = \frac{\overline{v'(\xi_o, y, t+\tau)p'(\xi_m, t)}}{U_e p_{\text{rms}}} \tag{4}$$

where, u' and v' are the streamwise and normal fluctuations of velocity and p' the surface-pressure fluctuations; ξ_o and ξ_m are the streamwise position of the cross wire and of a particular microphone, respectively; y is the distance normal to the surface of the airfoil when the cross wire is over the airfoil or the distance normal to the airfoil centerline when the cross wire is in the wake; τ is the time delay between the signals; U_e is the velocity at the edge of the boundary layer at the cross-wire location; and p_{rms} is the root mean square of the pressure fluctuations measured by the microphone. For a given cross-wire streamwise location (ξ_o) and for each microphone (ξ_m), two contour plots $R_{up}(\tau, y)$ and $R_{vp}(\tau, y)$ have been generated.

Figure 14 shows the contour plots of the temporal cross-correlation coefficient between u' and v' at 2 mm downstream of the blunt TE, i.e., in the wake ($x/C = 1.01$), and p' from microphones p_1 ($x/C = 0.99$) on the suction side and p_{1ps} ($x/C = 0.99$) on the pressure side for $Re_c = 2 \times 10^5$. Note that this notation is used to denote the upper and lower sides of the airfoil with the understanding that since the airfoil is symmetric, at 0° AOA there are no suction and pressure sides. The abscissa represents a dimensionless time delay $\tau U_e/\delta^*$ and the ordinate, the distance of the cross-wire traverse above and below the airfoil centerline, normalized by δ^*. The velocity at the edge of the boundary layer (or wake deficit), U_e and δ^* correspond to the cross-wire streamwise location. The boundary-layer thickness δ has been indicated in Fig. 14a as a reference. In all the plots, the dominance of the periodic vortical disturbance originated in the separated shear layer upstream of the TE is observed. The possible vortex shedding due to the bluntness of the TE is masked by the stronger vortex shedding from the separated and reattached laminar boundary layer. The period of the disturbance indicated by τ in the plots corresponds to a normalized value $\tau U_e/\delta^*$ of approximately 16, which is associated with a frequency of ≈200 Hz, similar to the frequency of the peak in the wall-pressure spectra of Fig. 13. As indicated earlier, the origin of the disturbance seems to be in the T-S waves that are inherent in a laminar boundary layer before undergoing transition and that in this case, interact with the K-H instabilities from the separated shear layer. The effect of the periodic vortical disturbance is seen to extend across the boundary layer

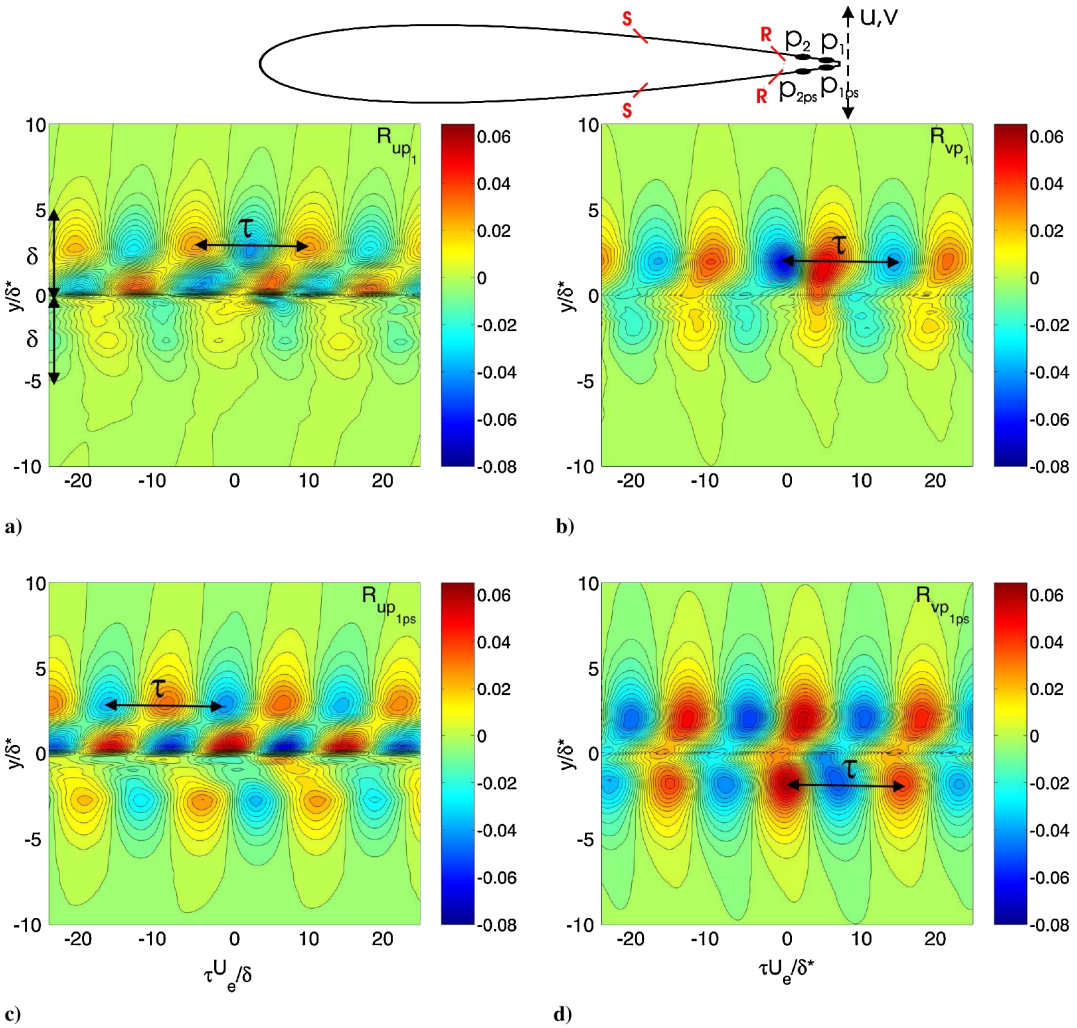

Fig. 14 Contour plots of cross-correlation coefficient between u' and v' at 2 mm ($x/C = 1.01$) downstream of the blunt TE in the wake and p' from microphones p_1 on the suction side and p_{1ps} on the pressure side, at $Re_c = 2 \times 10^5$. S and R indicate the approximate location of the separation and reattachment points.

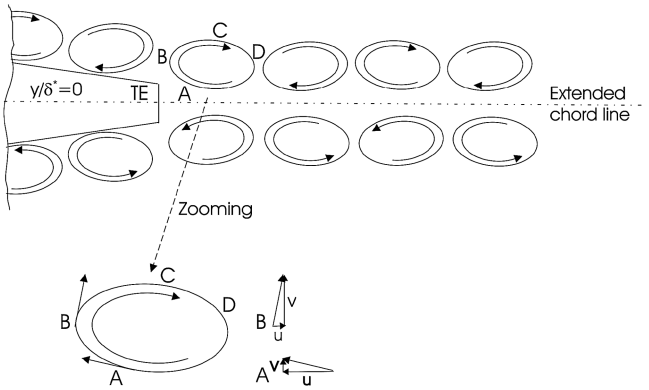

Fig. 15 Sketch of the vortex shedding from the separated shear layer upstream of the trailing edge.

($\delta \approx 5\delta^*$) and this disturbance is the dominant wall-pressure-generating flow structure for the low-Re_c case.

From the contour plots in Fig. 14, it can be observed that the mechanism seems stronger on the suction side than on the pressure side of the airfoil, i.e., in $R_{up_{1ps}}$ (Fig. 14c), the cross-correlation levels are still stronger on the upper part of the plot, despite p_{1ps} is on the pressure side. Because of the complexity of the mechanism and its likely dependence on external factors such as installation effects, surface finish, etc., it is not surprising to observe differences in its strength on the different sides of the airfoil. Furthermore, the authors surmise that it could be due to the acoustic-feedback loop between the TE and an upstream location described in the introduction and in Sec. III.E. Because of some external factor like surface roughness, this acoustic-feedback loop could be stronger on the suction side but affect the pressure-side microphones close to the TE. Since this mechanism would then influence more strongly the rolling vortices from the suction-side shear layer, this could explain the higher correlation between the velocities above the airfoil midcenterline and the microphone on the pressure side.

The difference in the position of the traverse where the highest levels are reached between R_{up_1} and R_{vp_1} is believed to be due to the shape of the vortical structures shed from the separated shear layer upstream of the TE. Figure 15 illustrates the vortex shedding from the separated shear layer. In points like A, which are closer to the extended chord line ($y \approx 0$), the streamwise component of the velocity is larger than the normal component of the velocity. In contrast, in points like B, further away from the chord line, the normal component of the velocity is higher. This is believed to explain the highest levels of cross-correlation between u' and p' closer to the extended chord line. Between $y/\delta^* = 2.5$ and 4, the cross-correlations levels between u' and p' are also rather high (point C) and have a different sign. This seems to be the reason why for a given $\tau U_e/\delta^*$, the R_{up} cross-correlation had opposite sign further away from the chord line than close to it. Similarly, in points like D, the cross-correlation between v' and p' is also high, but with opposite sign to that in B. That is why a succession of positive and negative vertical lobes were observed in the R_{vp} plots.

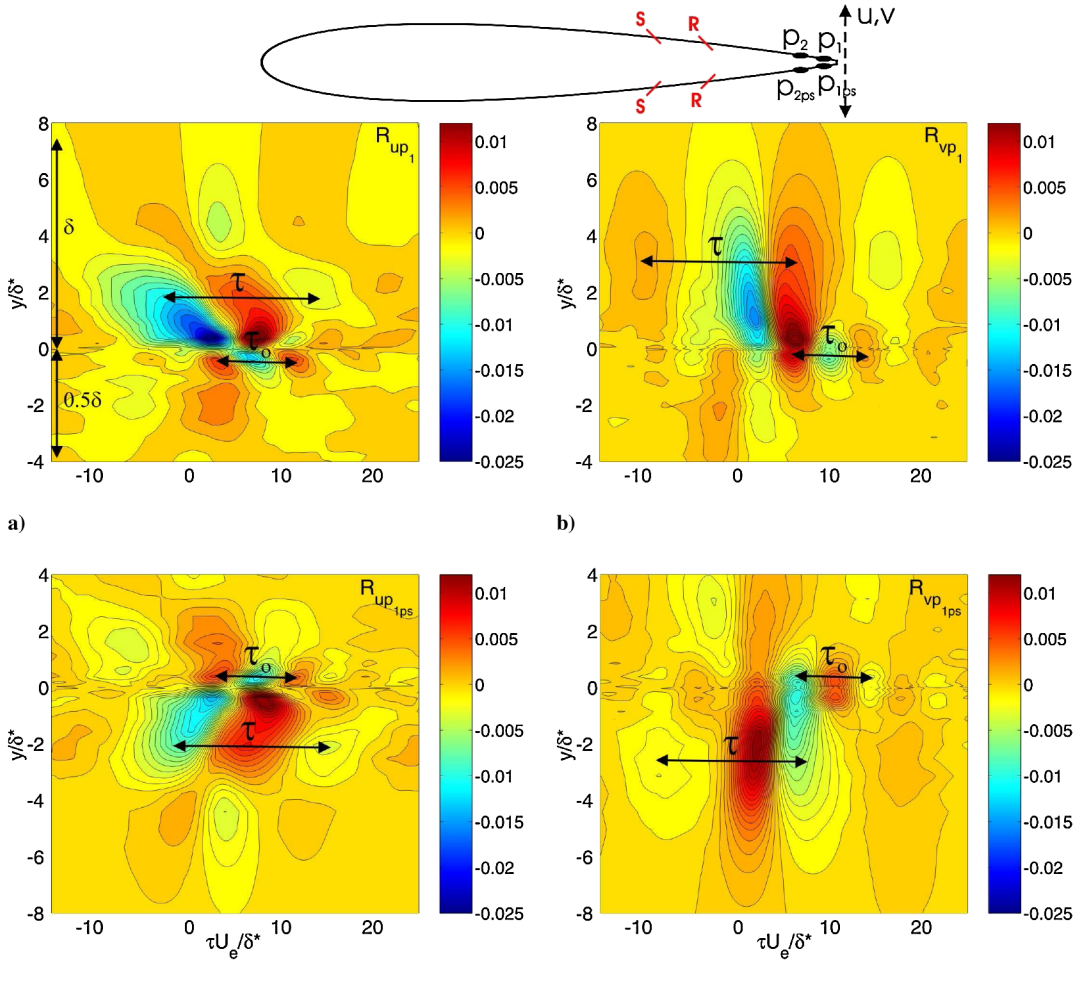

Fig. 16 Contour plots of cross-correlation coefficient between u' and v' at 2 mm ($x/C = 1.01$) downstream of the blunt TE in the wake and p' from microphones p_1 on the suction side and p_{1ps} on the pressure side, at $Re_c = 4 \times 10^5$. S and R indicate the approximate location of the separation and reattachment points.

Figure 16 shows the temporal cross-correlation coefficient between u' and v' at 2 mm downstream of the blunt TE in the wake ($x/C = 1.01$) and p' from microphones p_1 ($x/C = 0.99$) on the suction side and p_{1ps} ($x/C = 0.99$) on the pressure side for $Re_c = 4 \times 10^5$. Two different quasi-periodic vortex shedding mechanisms are observed in the plots. First, the vortex shedding associated with the blunt TE is indicated by τ_o and corresponds to a normalized value, $\tau U_e/\delta^*$, of about 8.5 (associated with a frequency of $\approx$1400 Hz). This quasi-periodic pattern associated with the unsteady vortex shedding from the TE is illustrated in the form of maxima (positive correlation) and minima (negative correlation) values of cross-correlation coefficient in a repetitive sequence behind the TE (values of y/δ^* near 0). It has been called quasi-periodic to distinguish it from the periodic, more coherent vortex shedding found in a von Karman street that is shed from a cylinder. The "quasi-periodicity" is also reflected in the fact that the cross-correlation associated with this pattern decays as the time delay τ increases.

The second quasi-periodic vortex shedding observed (indicated by τ) is due to the disturbances shed from the separated shear layer upstream of the TE. Similar repetitive sequence of positive and negative values of cross-correlation coefficient can be observed, this time extended across the boundary layer (or wake deficit) ($0 < y/\delta^* < 7$ or $0 > y/\delta^* > -7$ when correlating with p_1 or with p_{1ps}, respectively). It can be seen that it corresponds to a larger value of normalized time delay than the vortex shedding from the blunt TE, τ_o, since it is associated with lower frequencies. Indeed, τ corresponds to a $\tau U_e/\delta^*$ of about 17.5, that is associated with a frequency of 690 Hz, which is approximately the centered frequency of the hump observed in the wall-pressure spectra of Fig. 13. As discussed earlier, this hump is related to the interaction between the instabilities from the laminar boundary layer upstream (T-S) and those from the separated shear layer (K-H), which for this higher Re_c results in disturbances more broadband in nature than the more tonal structures observed at the lower Re_c.

The first mechanism, the vortex shedding from the blunt TE, is a local feature associated with the bluntness of the edge, whereas the vortex shedding from the separated shear layer extends across most of the boundary-layer thickness.

These two quasi-periodic vortical disturbances are the main mechanisms responsible for the wall-pressure generation for this high-Re_c case. Since the TE vortex shedding has a local effect, it affects mainly the surface pressure generated near the TE.

This investigation has been further complemented in Garcia-Sagrado and Hynes [56], in which a stochastic estimation technique has been applied to the simultaneously measured data of velocity and surface pressure, providing further information about the nature and evolution of the wall-pressure-generating structures. Moreover, in Garcia-Sagrado and Hynes [39], an analysis of the wall-pressure sources near the TE under turbulent boundary layers developing on the surface of a NACA0012 airfoil has been carried out.

IV. Conclusions

Laminar flow separation and flow-induced noise and vibration mechanisms have been investigated on a NACA0012 airfoil for two different flow conditions ($Re_c = 2 \times 10^5$ and 4×10^5). In particular, the mechanisms of narrowband and tonal noise due to vortex shedding from the instability waves of separated laminar boundary layers and the narrowband noise due to the vortex shedding from blunt trailing edges have been investigated from an aerodynamic point of view.

Simultaneous measurements have been presented of the unsteady surface-pressure fluctuations and of the velocity field, especially in the region close to the trailing edge. These detailed measurements have provided further understanding about laminar separated flows and about the relationship between the velocity and wall-pressure fields and thus about the flow structures responsible for the wall-pressure generation. These flow structures comprise the sources of the wall-pressure field, which are closely related to the sources of the radiated noise.

Boundary-layer mean velocity and turbulence intensity profiles indicated a laminar boundary layer that separated in the second half of the airfoil, due to the adverse pressure gradient, and reattached upstream of the TE for the two Re_c investigated. For the lower Re_c, the separation occurred earlier and the reattachment took place closer to the TE, resulting in a longer separation bubble. Oil and dye visualization confirmed the existence of a separated boundary layer that reattached upstream of the TE for the two flow conditions studied. The flow underwent transition along the separated shear layer with transition occurring earlier for the high Re_c. Analysis of the traces and spectra from the velocity and surface-pressure fluctuations was critical in the identification of the onset of transition in these separated flows.

Cross-correlations between velocity and surface pressure near the TE region provided information about the dominant wall-pressure-generating flow disturbances. The rolling vortices from the separated shear layer were identified as the dominant wall-pressure-generating structures, and hence the sources of the wall-pressure fluctuations, and were found to be distributed along the boundary layer (after reattachment). These rolling vortices were tonal in nature (periodic pattern) for the low Re_c and more broadband (quasi-periodic pattern) for the high Re_c. This was due to the proximity of the transition point to the separation point for the high Re_c and hence the presence of different frequencies associated with turbulent structures appearing during the transition process.

For the low Re_c, a main peak observed in the wall-pressure power spectral density of all microphones at approximately 200 Hz was found to be related to the periodical vortical structures originated in the separated shear layer. This dominant peak was also identified to be associated with the Tollmien–Schlichting (T-S) instabilities inherent in a laminar boundary layer. These disturbances interacted with the Kelvin–Helmholtz (K-H) instabilities from the separated shear layer, resulting in a complex mechanism. It is surmised that the second peak in the spectra at approximately 230 Hz is related to the K-H instabilities. At this low Re_c, evidence of an acoustic-feedback loop was observed, in which instability waves convecting over the trailing edge generate acoustic waves that propagate upstream and generate further instability waves. In the high-Re_c scenario, a hump was present in the wall-pressure power spectral density of the microphones (centered at around 600 or 700 Hz), which also seemed due to the T-S instabilities that got amplified in the separated shear layer and interacted with the K-H instabilities. However, due to the transition point occurring very close to the separation point in this case, both instabilities interacted with additional frequencies from the transition process resulting in such a hump instead of individual distinguishable frequencies (peaks in the spectra).

Unsteady vortex shedding was observed behind the blunt TE from the cross-correlation between the velocity in the wake and the pressure from the microphones closest to the TE on both sides of the airfoil. For the high Re_c, this was also noted as a small hump in the wall-pressure power spectral density of the microphone closest to the TE at approximately 1400 Hz. For the low Re_c, no clear evidence of vortex shedding from the TE could be identified because the stronger vortex shedding from the separated shear layer seems to conceal this phenomena.

Acknowledgments

This work has been funded by the U.K. Department of Trade and Industry under the Modelling and Simulation of Turbulence and Transition for Aerospace (MSTTAR) Defence and Aerospace Research Partnership (DARP) program. Ana Garcia-Sagrado also gratefully acknowledges the financial support from the Zonta International Amelia Earhart Fellowship. The MSTTAR DARP was supported by Rolls-Royce plc and BAE Systems. The authors are grateful for fruitful discussions with Ahmed Naguib and his students Mohamed Daoud and Laura Hudy from Michigan State University. Their advice and help is greatly appreciated. Special thanks for their support to Phil Joseph, Neil Sandham, Tze Pei Chong, and Richard Sandberg from the University of Southampton and John Coupland and Philip Woods from Rolls-Royce and BAE Systems, respectively. The

authors wish to thank Gavin Ross for his outstanding technical help with the airfoil model instrumentation and the experimental facility.

References

[1] Hatman, A., and Wang, T., "A Prediction Model for Separated-Flow Transition," ASME International, Paper 98-GT-237, 1998.

[2] Johnson, M., "A Bypass Transition Model for Boundary Layers," *Journal of Turbomachinery*, Vol. 116, 1994, pp. 759–764. doi:10.1115/1.2929470

[3] Solomon, W. J., Walker, G. J., and Gostelow, J. P., "Transition Length Prediction for Flows with Rapidly Changing Pressure Gradients," *Journal of Turbomachinery*, Vol. 118, 1996, pp. 744–751. doi:10.1115/1.2840930

[4] Volino, R., and Hultgren, L., "Measurements in Separated and Transitional Boundary Layers Under Low-Pressure Turbine Airfoil Conditions," *Journal of Turbomachinery*, Vol. 123, 2001, pp. 189–197. doi:10.1115/1.1350408

[5] Fitzgerald, E., and Mueller, T., "Measurements in a Separation Bubble on an Airfoil Using Laser Velocimetry," *AIAA Journal*, Vol. 28, No. 4, 1990, pp. 584–592. doi:10.2514/3.10433

[6] Brendel, M., and Mueller, T., "Boundary Layer Measurements on an Airfoil at Low Reynolds Numbers," AIAA Paper 87-0495, 1987.

[7] O'Meara, M. M., and Mueller, T. J., "Laminar Separation Bubble Characteristics on an Airfoil at Low Reynolds Numbers," *AIAA Journal*, Vol. 25, No. 8, 1987, pp. 1033–1041. doi:10.2514/3.9739

[8] Lang, M., Rist, U., and Wagner, S., "Investigations on Controlled Transition Development in a Laminar Separation Bubble by Means of LDA and PIV," *Experiments in Fluids*, Vol. 36, 2004, pp. 43–52. doi:10.1007/s00348-003-0625-x

[9] Ol, M. V., Hanff, E., McAuliffe, B., Scholz, U., and Kaehler, C., "Comparison of Laminar Separation Bubble Measurements on a Low Reynolds Number Airfoil in Three Facilities," 35th AIAA Fluid Dynamics Conference and Exhibit, Toronto, AIAA Paper 2005-5149, 2005.

[10] Raffel, M., Favier, D., Berton, E., Rondot, C., Nsimba, M., and Geissler, M., "Micro-PIV and ELDV Wind Tunnel Investigations of the Laminar Separation Bubble Above a Helicopter Blade Tip," *Measurement Science and Technology*, Vol. 17, 2006, pp. 1652–1658. doi:10.1088/0957-0233/17/7/003

[11] Burgmann, S., Bruecker, S., and Schroeder, W., "Scanning PIV Measurements of a Laminar Separation Bubble," *Experiments in Fluids*, Vol. 41, 2006, pp. 319–326. doi:10.1007/s00348-006-0153-6

[12] Hu, H., and Yang, Z., "An Experimental Study of the Laminar Flow Separation on a Low-Reynolds-Number Airfoil," *Journal of Fluids Engineering*, Vol. 130, 2008, Paper 051101. doi:10.1115/1.2907416

[13] Brooks, T. F., Pope, D. S., and Marcolini, M. A., "Airfoil Self-Noise and Prediction," NASA Ref. Publ. 1218, 1989.

[14] Roger, M., and Moreau, S., "Broadband Self-Noise from Loaded Fan Blades," *AIAA Journal*, Vol. 42, No. 3, 2004, pp. 536–544. doi:10.2514/1.9108

[15] Kinns, R., and Bloor, C., "Hull Vibration Excitation Due to Monopole and Dipole Propeller sources," *Journal of Sound and Vibration*, Vol. 270, 2004, pp. 951–980. doi:10.1016/S0022-460X(03)00641-2

[16] Ciappi, E., Magionesi, F., Rosa, S. D., and Franco, F., "Hydrodynamic and Hydroelastic Analyses of a Plate Excited by the Turbulent Boundary Layer," *Journal of Fluids and Structures*, Vol. 25, 2009, pp. 321–342. doi:10.1016/j.jfluidstructs.2008.04.006

[17] Ciappi, E., and Magionesi, F., "Characteristics of Turbulent Boundary Layer Pressure Spectra for High-Speed Vessels," *Journal of Fluids and Structures*, Vol. 21, 2005, pp. 321–333. doi:10.1016/j.jfluidstructs.2005.07.006

[18] Desqesnes, G., Terracol, M., and Sagaut, P., "Numerical Investigation of the Tone Noise Mechanism over Laminar Airfoils," *Journal of Fluid Mechanics*, Vol. 591, 2007, pp. 155–182.

[19] Sandberg, R. D., Jones, L., Sandham, N., and Joseph, P., "Direct Numerical Simulation of Tonal Noise Generated by Laminar Flow Past Airfoils," *Journal of Sound and Vibration*, Vol. 320, 2009, pp. 838–858. doi:10.1016/j.jsv.2008.09.003

[20] Jones, L., Sandberg, R., and Sandham, N., "Stability and Receptivity Characteristics of a Laminar Separation Bubble on an Airfoil," *Journal of Fluid Mechanics*, Vol. 648, 2010, pp. 257–296. doi:10.1017/S0022112009993089

[21] Howe, M., "A Review of the Theory of Trailing Edge Noise," *Journal of Sound and Vibration*, Vol. 61, 1978, pp. 437–465. doi:10.1016/0022-460X(78)90391-7

[22] Amiet, R., "Noise Due to Turbulent Flow Past a Trailing Edge," *Journal of Sound and Vibration*, Vol. 47, 1976, pp. 387–393. doi:10.1016/0022-460X(76)90948-2

[23] Brooks, T. F., and Hodgson, T. H., "Trailing Edge Noise Prediction from Measured Surface Pressures," *Journal of Sound and Vibration*, Vol. 78, 1981, pp. 69–117. doi:10.1016/S0022-460X(81)80158-7

[24] Yu, J. C., and Joshi, M. C., "On Sound Radiation from the Trailing Edge of an Isolated Airfoil in a Uniform Flow," AIAA Paper 79-0603, 1979.

[25] Rozenberg, Y., Roger, M., and Moreau, S., "Rotating Blade Trailing-Edge Noise: Experimental Validation of Analytical Model," *AIAA Journal*, Vol. 48, 2010, pp. 951–962. doi:10.2514/1.43840

[26] Bertagnolio, F., Madsen, H. A., and Bak, C., "Trailing Edge Noise Model Validation and Application to Airfoil Optimization," *Journal of Solar Energy Engineering*, Vol. 132, 2010, Paper 031010. doi:10.1115/1.4001462

[27] Wang, M., Moreau, S., Iaccarino, G., and Roger, M., "LES Prediction of Wall-Pressure Fluctuations and Noise of a Low-Speed Airfoil," *International Journal of Aeroacoustics*, Vol. 8, 2009, pp. 177–198. doi:10.1260/147547208786940017

[28] Agarwal, N. K., and Simpson, R. L., "A New Technique for Obtaining the Turbulent Pressure Spectrum from the Surface Pressure Spectrum," *Journal of Sound and Vibration*, Vol. 135, No. 2, 1989, pp. 346–350. doi:10.1016/0022-460X(89)90731-1

[29] Helal, H. M., Casarella, M. J., and Farabee, T. M., "An Application of Noise Cancellation Techniques to the Measurement of Wall Pressure Fluctuations in a Wind Tunnel," *ASME Winter Annual Meeting*, ASME International, Rept. H00563, 1989, pp. 49–59.

[30] Naguib, A. M., Gravante, S. P., and Wark, C., "Extraction of Turbulent Wall-Pressure Time-Series Using an Optimal Filtering Scheme," *Experiments in Fluids*, Vol. 22, 1996, pp. 14–22. doi:10.1007/BF01893301

[31] Rozenberg, Y., Roger, M., Guedel, A., and Moreau, S., "Rotating Blade Self Noise: Experimental Validation of Analytical Models," 12th AIAA/CEAS Aeroacoustics Conference, Cambridge, MA, AIAA Paper 2006-2563, 2007.

[32] Rozenberg, Y., Roger, M., and Moreau, S., "Effect of Blade Design at Equal Loading on Broadband Noise," 12th AIAA/CEAS Aeroacoustics Conference, Cambridge, MA, AIAA Paper 2006-2563, 2006.

[33] Blake, W., *Mechanics of Flow-Induced Sound and Vibration*, Applied Mathematics and Mechanics, Vol. 17, 1986.

[34] Mish, P., "Mean Loading and Turbulence Scale Effects on the Surface Pressure Fluctuations Occurring on a NACA0015 Airfoil Immersed in Grid Generated Turbulence," M.S. Thesis, Virginia Polytechnic Inst. and State Univ., Blacksburg, VA, 2001.

[35] Bearman, P., "Correction for the Effect of Ambient Temperature Drift on Hotwire Measurements in Incompressible Flow," *DISA Information*, Vol. 11, 1971, pp. 25–30.

[36] Cox, R., "Wall Neighborhood Measurements in Turbulent Boundary Layers Using a Hot-Wire Anemometer," Aeronautical Research Council, Rept. 19191, 1957.

[37] Champagne, F. H., Sleicher, C. A., and Wehrmann, O. H., "Turbulence Measurements with Inclined Hot-Wires. Part 1. Heat Transfer Experiments with Inclined Hot-Wire," *Journal of Fluid Mechanics*, Vol. 28, 1967, pp. 153–75.

[38] Champagne, F. H., and Sleicher, C. A., "Turbulence Measurements with Inclined Hot-Wires. Part 2. Hot-Wire Response," *Journal of Fluid Mechanics*, Vol. 28, 1967, pp. 177–182. doi:10.1017/S0022112067001971

[39] Garcia-Sagrado, A., and Hynes, T., "Wall Pressure Sources Near an Airfoil Trailing Edge Under Tripped Boundary Layers," *Journal of Fluids and Structures*, (to be published).

[40] Schlichting, H., *Boundary-Layer Theory*, A McGraw–Hill, New York, 1979.

[41] Young, A. D., *Boundary Layers*, BSP Professional Books, Oxford, 1989.

[42] Lang, M., Rist, U., and Wagner, S., "Investigations on Disturbance Amplification in a Laminar Separation Bubble by Means of LDA and PIV," *Experiments in Fluids*, Vol. 36, 2004, pp. 43–52. doi:10.1007/s00348-003-0625-x

[43] Thwaites, B., "Approximate Calculation of the Laminar Boundary Layer," *Aeronautical Quarterly*, 1949, pp. 245–280.

[44] Volino, R., "Separated Flow Transition Under Simulated Low-Pressure Turbine Airfoil Conditions–Part 2: Turbulence Spectra," *Transactions*

of the ASME, Vol. 124, 2002, pp. 656–664.
[45] Lin, J., and Pauley, L., "Low-Reynolds-Number Separation on an Airfoil," *AIAA Journal*, Vol. 34, No. 8, 1996, pp. 1570–1577. doi:10.2514/3.13273
[46] Hatman, A., and Wang, T., "Separated-Flow Transition. Part 1—Experimental Methodology and Mode Classification," ASME International Paper 98-GT-461, 1998.
[47] Hatman, A., and Wang, T., "Separated-Flow Transition. Part 2—Experimental Results," ASME International, Paper 98-GT-462, 1998.
[48] Mayle, R., "The Role of Laminar-Turbulent Transition in Gas Turbine Engines," *Journal of Turbomachinery*, Vol. 113, 1991, pp. 509–537. doi:10.1115/1.2929110
[49] Hatman, A., and Wang, T., "Separated-Flow Transition. Part 3—Primary Modes and Vortex Dynamics," ASME International Paper 98-GT-463, 1998.
[50] Roberts, S., and Yaras, M., "Large-Eddy Simulation of Transition in a Separation Bubble," *Transactions of the ASME*, Vol. 128, 2006, pp. 232–238.
[51] Lou, W., and Hourmouziadis, J., "Separation Bubbles Under Steady and Periodic-Unsteady Main Flow Conditions," *Transactions of the ASME*, Vol. 122, 2000, pp. 634–643.
[52] Stieger, R., "The Effects of Wakes on Separating Boundary Layers in Low Pressure Turbines," Ph.D. Thesis, Univ. of Cambridge, Cambridge, England, U.K., 2002.
[53] Walker, G., "Transitional Flow on Axial Turbomachine Blading," *AIAA Journal*, Vol. 27, No. 5, 1989, pp. 595–602. doi:10.2514/3.10150
[54] Brooks, T., Pope, D., and Marcolini, M., "Airfoil Self-Noise and Prediction," NASA Ref. Publ. 1218, 1989.
[55] Oerlemans, S., and Migliore, P., "Aeroacoustic Wind Tunnel Tests of Wind Turbine Airfoils," AIAA Paper 2004-3042, 2004.
[56] Garcia-Sagrado, A., and Hynes, T., "Stochastic Estimation of Flow Near the Trailing Edge of a NACA0012 Airfoil," *Experiments in Fluids* (to be published). doi:10.1007/s00348-011-1071-9

D. Papamoschou
Associate Editor